The Astrophysical Journal, 974:132 (20pp), 2024 October 10 https://doi.org/10.3847/1538-4357/ad6f05

Tilted Disk Precession and Negative Superhumps in HS 2325+8205: A Multiwindow Analysis

Qi-Bin Sun[1,2], Sheng-Bang Qian[1,2], Li-Ying Zhu[3,4], Qin-Mei Li[5], Min-Yu Li[3,4], and Ping Li[3,4]
[1] Department of Astronomy, School of Physics and Astronomy, Yunnan University, Kunming 650091, People's Republic of China; qsb@ynao.ac.cn
[2] Key Laboratory of Astroparticle Physics of Yunnan Province, Yunnan University, Kunming 650091, People's Republic of China
[3] Yunnan Observatories, Chinese Academy of Sciences, Kunming 650216, People's Republic of China
[4] University of Chinese Academy of Sciences, No. 19(A) Yuquan Road, Shijingshan District, Beijing, People's Republic of China
[5] Department of Physics, College of Physics, Guizhou University, Guiyang, 550025, People's Republic of China
Received 2024 July 7; revised 2024 August 6; accepted 2024 August 12; published 2024 October 9

Abstract

Tilted disk precession exists in different objects. Negative superhumps (NSHs) in cataclysmic variable stars are believed to arise from the interaction between the reverse precession of a tilted disk and the streams from the secondary star. Utilizing Transiting Exoplanet Survey Satellite photometry, we present a comprehensive investigation into the tilted disk precession and NSHs in the dwarf nova (DN) HS 2325+8205, employing eclipse minima, eclipse depths, NSH frequencies, and NSH amplitudes and the correlation between them as the windows. We identified NSHs with a period of 0.185671(17) day in HS 2325+8205. The NSH frequency exhibits variability with a period of 3.943(9) days, akin to the tilted disk precession period validated in nova-like stars (SDSS J0812) and intermediate polars (IPs; TV Col). The $O-C$ of the eclipse minima were similarly found to vary cyclically in a period of 4.135(5) days, characterized by a faster rise than fall. Furthermore, the NSH amplitude exhibits complex and diverse variations, which may be linked to changes in the disk radius, the mass transfer rate, and the apparent area of the hot spot. For the first time in DNe, we observe biperiodic variations in eclipse depth ($P_1 = 4.131(4)$ days and $P_2 = 2.065(2)$ days $\approx P_{\rm prec}/2$) resembling those seen in IPs, suggesting that variations with P_2 are not attributable to an accretion curtain, as previously suspected. Moreover, NSH amplitude and eclipse depth decrease with increasing NSH frequency, while NSH amplitude correlates positively with eclipse depth. These complex variations observed across multiple observational windows provide substantial evidence for the understanding of tilted disk precession and NSHs.

Unified Astronomy Thesaurus concepts: Cataclysmic variable stars (203); Semi-detached binary stars (1443); Dwarf novae (418)

1. Introduction

Superorbital signals (SORs) have been found in cataclysmic variable stars (CVs) such as TV Col (Q.-B. Sun et al. 2024a; $P_{\rm sor} \sim 4$ days), active galactic nuclei, black hole binaries like SS 433 (S. B. Foulkes et al. 2010; $P_{\rm sor} \sim 162$ days), and X-ray binaries such as Her X-1 (R. Giacconi et al. 1973; $P_{\rm sor} \sim 35$ days). These signals are generally believed to originate from the reverse precession of tilted accretion disks. Evidence comes from the discovery of reverse precession in jets (e.g., R. M. Hjellming & K. J. Johnston 1981; A. Caproni & Z. Abraham 2004; Z. Abraham 2018; Y. Cui et al. 2023). The precession period of the jet in M87 was measured to be $P_{\rm prec} \sim 11$ yr (Y. Cui et al. 2023), and the precession timescale of the active galactic nucleus 2MASX J12032061+1319316 was estimated to be $P_{\rm prec} \sim 10^5$ yr (K. Rubinur et al. 2017).

CVs exhibit SORs with periods of only a few days, believed to originate from the reverse precession of tilted disks (e.g., J. I. Katz 1973; P. Barrett et al. 1988; D. Harvey et al. 1995; M. A. Wood et al. 2009). They have short precession timescales and numerous examples of precession signals (e.g., A. Bruch 2022, 2023a, 2023b; Q.-B. Sun et al. 2022; S. Y. Stefanov & A. K. Stefanov 2023). Therefore, CVs provide an ideal experimental environment for studying tilted disk precession in astrophysics. Negative superhumps (NSHs) in CVs, with periods several percent shorter than the orbital period, are thought to result from interactions between the streams from the secondary star and the reverse precession of tilted disks (e.g., J. M. Bonnet-Bidaud et al. 1985; D. Harvey et al. 1995; J. Patterson 1999). The relationship $1/P_{\rm prec} = 1/P_{\rm sor} = 1/P_{\rm nsh} - 1/P_{\rm orb}$ exists, where $P_{\rm prec}$ is the precession period.

Evidence for the tilted disk precession has been found, with the surprising agreement of the SORs with predictions of the tilted disk precession period ($P_{\rm prec} \simeq P_{\rm sor}$) being the most important evidence. Other evidence includes the eclipse minima, the eclipse depth, the eclipse width, and the NSH amplitude with periodic variations similar to the theoretical tilted disk precession period ($P_{\rm prec} \simeq P_{\rm sor} \simeq P_{O-C,\rm eclipse} \simeq P_{\rm depth,eclipse} \simeq P_{\rm width,eclipse} \simeq P_{\rm amplitude,\ NSHs}$). NSHs are thought to originate from the interaction of the streams with the tilted disk precession, and the main observational evidence for this is $1/P_{\rm nsh} \simeq 1/P_{\rm sor} + 1/P_{\rm orb}$. Some authors have reproduced NSHs based on smooth particle hydrodynamics within the framework of this model (e.g., M. M. Montgomery 2009; M. A. Wood et al. 2009; M. Kimura & Y. Osaki 2021). The finding that the NSH amplitude varies as the tilted disk precession is very important evidence. However, this observational evidence is still lacking.

Recently, we conducted an extensive study of tilted disk precession in CVs using space telescope data, focusing on NSHs as a key indicator (e.g., Q.-B. Sun et al. 2023b, 2023a, 2024b, 2024a). Dwarf nova (DN) outbursts are commonly attributed to thermal instabilities in accretion disks, while

NSHs are believed to arise from interactions between tilted disk precession and streams from secondary stars. However, the combination of thermally unstable and tilted disks remains poorly understood. We observed in DN systems AH Her, ASAS J1420, TZ Per, and V392 Hya that NSH amplitudes vary with outburst phases (Q.-B. Sun et al. 2023a, 2024b), suggesting a significant link between NSHs and DN outbursts as a valuable avenue for studying accretion disk instability and NSH origins. Additionally, we detected periodic variations in eclipse minima, eclipse depth, and NSH amplitudes consistent with the precession period of the tilted accretion disk in the nova-like star (NL) SDSS J0812 (Q.-B. Sun et al. 2023b). These findings provide strong evidence for a direct correlation between NSH origin and tilted disk precession. Subsequently, we confirmed these phenomena in the intermediate polar (IP) system TV Col, a prototype for NSH systems, and observed a biperiodic variation in eclipse depth, potentially linked to the dual accretion curtains of IPs (Q.-B. Sun et al. 2024a) and offering critical observational insights into tilted disk precession in CVs. Recent studies by A. Bruch (2024) have similarly identified a prevalence of periodic variations in observed minus calculated ($O-C$) diagrams and eclipse widths, consistent with the period of tilted disk precession.

HS 2325+8205, a long-period eclipsing DN (∼4.66 hr) initially discovered by O. Morgenroth (1936), has a rich observational history (e.g., O. Morgenroth 1936; H.-J. Hagen et al. 1995; A. Aungwerojwit et al. 2005; J. Shears et al. 2011; L. K. Hardy et al. 2017; Q.-B. Sun et al. 2023c) and is classified as a Z Cam–type DN due to its short recurrence period (S. Pyrzas et al. 2012). In our recent study, we identified quasiperiodic oscillations (QPOs) with a period of ∼2160 s during the peak of a long outburst, with the QPO intensity correlated with orbital phase (Q.-B. Sun et al. 2023c). Hence, we propose that studying the relationship between QPOs and orbital phase could offer valuable insights into their origins.

Although the tilted disk reverse precession model is widely used, the mechanism that leads to disk tilting and reverse precession is controversial. Fundamental questions, such as how the material streams from the secondary star interact with the accretion disk and the underlying physical processes at the point of contact, require more detailed exploration. SORs characterize tilted disk precession, but current studies indicate that SORs are not universally observed in systems with NSHs, particularly in DNe with NSHs (e.g., G. Ramsay et al. 2017; J. Court et al. 2020; Q.-B. Sun et al. 2023a, 2024b), posing a challenge to the tilted disk precession theory. HS 2325+8205, a DN with NSHs, presents new observational data. Utilizing eclipse minima, eclipse depths, NSH frequencies, and NSH amplitudes as investigative windows, we endeavor to explore potential evidence of tilted disk precession and validate whether phenomena observed in nonmagnetic CVs (NLs) and magnetic CVs (IPs) also manifest in DNe. This approach aims to provide invaluable observational insights for studies pertaining to tilted disk precession and NSHs.

The organization of this paper is outlined as follows. Section 2 introduces the photometric data obtained through the Transiting Exoplanet Survey Satellite (TESS) mission. In Section 3, we conduct an in-depth analysis of NSH frequency, NSH amplitude, and eclipse depth, as well as $O-C$ variations and QPOs. Section 4 delves into potential explanations for the observed changes. Finally, Section 5 presents the conclusions.

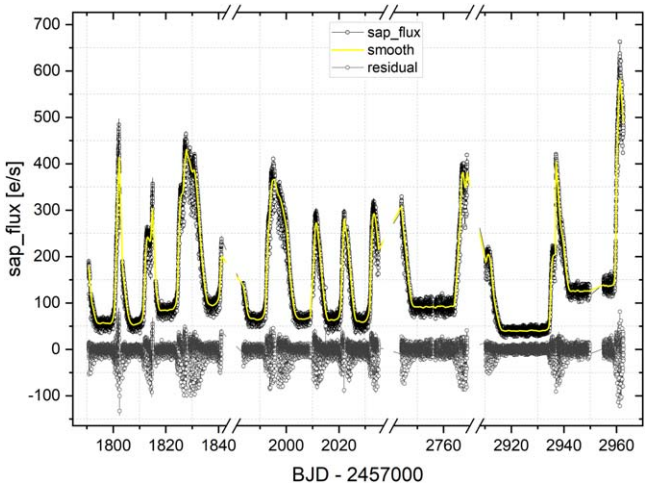

Figure 1. HS 2325+8205 light curve from TESS photometry. The yellow line is the LOWESS fit in order to remove the outburst trend.

Table 1
Journal of Observations

Sectors	Start Time (MBJD)	Start Time (UT)	End Time (MBJD)
18	58790.15713	2019-11-03	58814.51574
19	58815.58519	2019-11-28	58840.65031
25	58983.12924	2020-05-14	59008.80275
26	59009.76386	2020-06-09	59034.63223
53	59743.49271	2022-06-13	59768.47641
59	59909.76523	2022-11-26	59936.18870
60	59936.40397	2022-12-23	59962.08395

2. TESS Photometry

This paper harnesses data from TESS (G. Ricker et al. 2015), launched by NASA in 2018 and managed by MIT. NASA's Ames Research Center's Science Processing Operations Center (J. M. Jenkins et al. 2016) is responsible for processing TESS's calibrated data into light curves, providing both simple aperture photometry (SAP) and presearch data-conditioned simple aperture photometry light curves (for details, see J. D. Twicken et al. 2010 and K. Kinemuchi et al. 2012). Eventually, these data are transmitted to the Mikulski Archive for Space Telescopes.[6] Our research has already made significant progress in studying CVs utilizing TESS data (e.g., Q.-B. Sun et al. 2023a, 2023b, 2023c, 2024a, 2024b).

The photometric observations of HS 2325+8205 were conducted by the TESS mission, encompassing Sectors 18, 19, 25, 26, 53, 59, and 60 (refer to Table 1 and Figure 1 for details). Our recent research revealed the presence of QPOs during the peak of the long outbursts of HS 2325+8205, utilizing data from Sectors 18, 19, 25, and 26 (Q.-B. Sun et al. 2023c). Subsequently, fresh data from TESS were released, and the current study primarily focuses on analyzing the data obtained from Sectors 53, 59, and 60, particularly exploring the impact of the emerging NSHs and the accretion disk precession on the system.

[6] https://mast.stsci.edu/

Table 2
Frequency Analysis Results of Period04 for Different Curves of HS 2325+8205

Start and End Times[a] (day)	Sectors	Types[b]	Frequency (1 day^{-1})	Errors (1 day^{-1})	Period (day)	Errors (day)	Amplitude[f] (e s^{-1})	Errors[f] (e s^{-1})
1790.6586–1841.1504	18, 19	orb	5.1475	1.63E–04	0.194270	6.13E–06	6.629	0.099
		2*orb	10.2923	1.31E–04	0.097160	1.23E–06	8.253	0.099
1983.6307–2035.1323	25, 26	orb	5.1447	1.30E–04	0.194376	4.92E–06	7.111	0.086
		2*orb	10.2910	1.10E–04	0.097172	1.04E–06	8.421	0.086
2743.9942–2768.9765	53	orb	5.1472	5.79E–04	0.194281	2.19E–05	4.043	0.106
		nsh	5.3881	2.82E–04	0.185594	9.72E–06	8.298	0.106
		2*orb	10.2929	3.40E–04	0.097155	3.21E–06	6.892	0.106
2910.2667–2936.6888	59	orb	5.1437	7.74E–04	0.194412	2.93E–05	2.366	0.088
		nsh	5.3729	4.30E–04	0.186121	1.49E–05	4.264	0.088
		2*orb	10.2901	4.45E–04	0.097181	4.21E–06	4.113	0.088
2936.9055–2962.5841	60	orb	5.1476	7.65E–04	0.194265	2.89E–05	5.671	0.202
		nsh	5.3967	7.89E–04	0.185299	2.71E–05	5.500	0.202
		2*orb	10.2943	5.42E–04	0.097141	5.12E–06	8.003	0.202
2744.3160–2962.0519	53, 59, 60	fre	0.2536	5.81E–04	3.942596	9.03E–03	0.067	0.015
2744.3160–2768.4769	53	A1	0.2150	5.05E–03	4.651595	1.09E–01	2.350	0.520
2910.6340–2962.0519	59, 60	A2	0.2381	3.11E–03	4.200622	5.49E–02	1.416	0.411
2748.0497–2959.0980	53, 59, 60	$O-C$	0.2419	2.65E–04	4.134623	4.54E–03	0.0010	0.0001
2748.0497–2959.0980	53, 59, 60	depth1	0.2421	2.60E–04	4.131036	4.43E–03	2.618	0.260
2748.0497–2959.0980	53, 59, 60	depth2	0.4842	4.87E–04	2.065178	2.08E–03	1.413	0.263
2961.2563–2962.5730	60	QPO[c]	39.477	2.41E–02	2188.638	1.34E+00	7.054	0.407
1251.8247–1302.2254	K2(c18)	SDSS J0812[d]	0.3214	3.03E–03	3.111484	2.93E–02	0.092	0.026
2174.7567–2227.0064	32, 33	TV Col[e]	0.2555	1.93E–03	3.913435	2.96E–02	0.122	0.022

Notes.
[a] The units are BJD–2457000.
[b] The meanings of the different symbols are as follows: orb = orbital frequency, nsh = NSH frequency, 2*orb = second harmonic of the orbital frequency, fre = frequency of NSH frequency change, A1 = peak frequency of change in NSH amplitude in Sector 53, A2 = frequency of NSH amplitude change in Sectors 59 and 60, $O-C$ = signal of the $O-C$ curve change, depth1 = peak frequency of eclipse depth, depth2 = peak frequency of the residual from the first analysis (details in Section 3.6), and QPO = peak frequency of the QPO at the top of the outburst in Sector 60.
[c] The unit of the QPO's period is the second, and the other period units are days.
[d] Periodic analysis of the NSH frequency of SDSS J0812 (Q.-B. Sun et al. 2023b) from the 18th observational campaign of K2.
[e] Periodic analysis of the NSH frequency of TV Col (Q.-B. Sun et al. 2024a).
[f] The symbols fre, SDSS J0812, and TV Col have an amplitude unit of 1 day^{-1}, $O-C$ has an amplitude unit of days, and all the remaining amplitudes have a unit of e s^{-1}.

3. Analysis and Results

3.1. The Emergence of NSHs

To analyze the photometric data of HS 2325+8205 obtained by TESS, we employed the locally weighted regression (LOWESS) method (W. S. Cleveland 1979) to remove the outburst trend, as illustrated in Figure 1. The resulting residuals were segmented into five parts for frequency analysis using Period04 software (details in P. Lenz & M. Breger 2005). Sectors 18 and 19 are treated as one part, Sectors 25 and 26 as another, and the remaining 53, 59, and 60 as one part each (see Table 2 for the span of each part). This analysis revealed dominant orbital periods, NSHs, and twice the orbital harmonic signals. Notably, NSHs were detected specifically in sectors 53, 56, and 60, as shown in Figures 2(b) and (c). Further analysis excluding eclipse phases emphasized the prominence of NSHs. The average period of the NSHs was determined to be 0.185671(17) day, averaged over the three sectors (see Figure 2(c) and Table 2). The orbital period averaged over all five sectors was calculated as 0.194321 (18) day. This marks the first detection of NSHs in HS 2325 +8205. The excess was calculated as $\epsilon = -0.0445(2)$, where $\epsilon = (P_{\rm nsh} - P_{\rm orb})/P_{\rm orb}$. No SORs were identified in the light curve. The theoretical precession signal was calculated to be 4.171(17) days (0.240(1) day^{-1}, $1/P_{\rm prec} = 1/P_{\rm nsh} - 1/P_{\rm orb}$).

3.2. Parameter Extraction for NSHs

More recent studies have highlighted the complexity and variability of NSHs, where a single period is insufficient to describe its behavior. We observed periodic variations in NSH amplitude, $O-C$, and eclipse depth in NLs and IPs, and we aimed to verify this phenomenon in DN HS 2325+8205, where no SORs were found. If periodic variations similar to the tilted disk precession cycle were found, it would be possible to demonstrate that the tilted disk has not disappeared. Therefore, we employed a segmented fitting approach similar to Q.-B. Sun et al. (2023b, 2024a) to explore the evolution of NSHs.

NSHs were detected solely in Sectors 53, 56, and 60, with the corresponding SAP_flux light curve labeled LC#1 (see Figure 3(a)). The light curve after removing the outburst trend was denoted as LC#2 (see Figure 3(b)). The out-of-eclipse portion of LC#2 was divided into 91 segments, each spanning approximately 4 times the orbital period (~0.78 day, accounting for potential data gaps of varying durations; see Table A1). Following the methods of Q.-B. Sun et al. (2023b, 2024a), we initially attempted a segmented linear superposition sinusoidal model to fit the out-of-eclipse curve of LC#2 (depicted by blue circles in Figure 3(b)) but encountered poor fitting results during outburst peaks. Due to the persistent outburst presence in LC#1, which hindered accurate LOWESS trend removal per segment, we opted for a least-squares quadratic superimposed

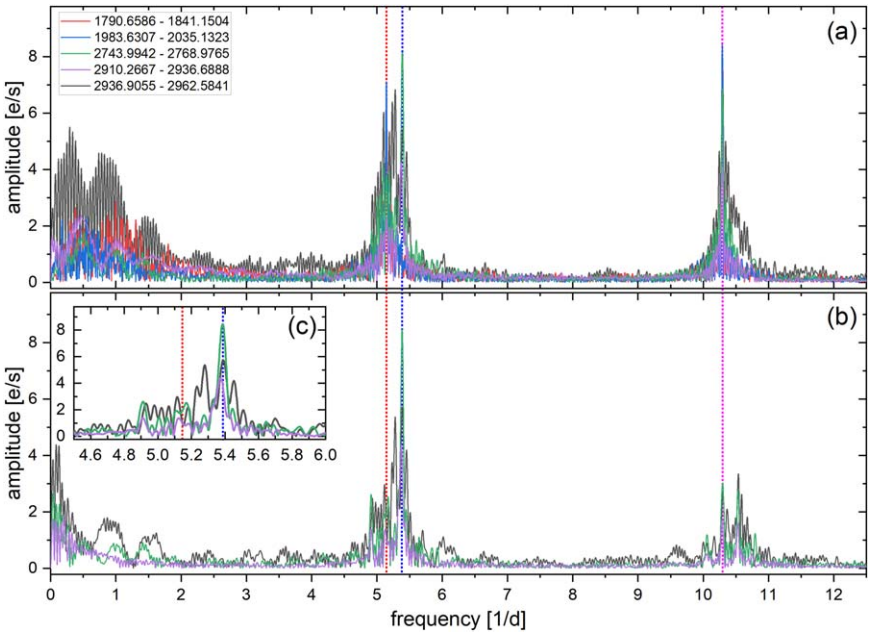

Figure 2. Frequency spectrograms of HS 2325+8205. (a) Results of the frequency analysis of the light curve after removing the outburst trend by dividing it into five separate parts (see Table 2); the time range in the legend is in units of BJD–2457000. (b) Results of the analysis of the curves after removing the outburst trend and eclipse for Sectors 53, 59, and 60. (c) Local zoomed-in view of plate (b); vertical red, blue, and magenta dashed lines correspond sequentially to the orbital frequency, the NSH frequency, and the twice harmonic of the orbital frequency (all averaged over different sectors).

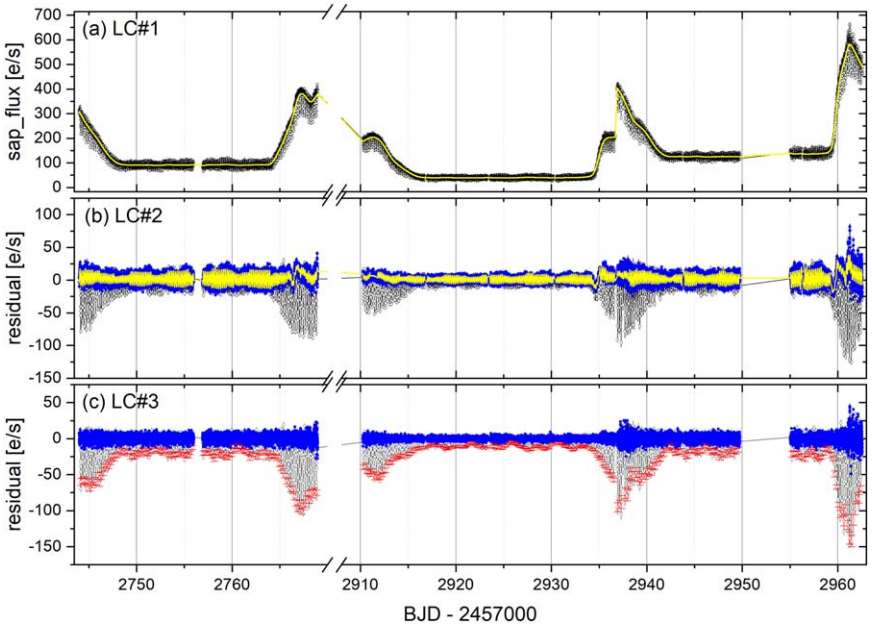

Figure 3. Segmented fitting process. (a) SAP_flux light curves (LC#1) for Sectors 53, 59, and 60; the yellow solid line is the LOWESS fit. (b) Residuals (LC#2) of the LOWESS fit to LC#1; the blue points are the out-of-eclipse curves, and the yellow solid line is the segmental fit to the out-of-eclipse curves. (c) Residuals (LC#3) obtained by subtracting the yellow solid line from all light curves in LC#2; the blue points are the out-of-eclipse curves, and the red points are the eclipse minima.

sinusoidal model without weighting to mitigate outburst effects:

$$\mathrm{Flux(BJD)} = Z + B \cdot \mathrm{BJD} + C \cdot \mathrm{BJD}^2 + A \cdot \sin(2\pi \cdot (\mathrm{freq} \cdot \mathrm{BJD} + p)). \quad (1)$$

Here, Z, B, C, A, freq, and p represent the fitted intercept, linear coefficients, quadratic coefficients, amplitude, frequency, and phase, respectively. The theoretical NSH curve derived from the segmental fit was subtracted from the LC#1 light curve to obtain LC#3, which represents the light curve after removing the NSH trend. The final fit results are depicted by the yellow solid line in Figure 3(b) and summarized in Table A1, providing crucial insights into NSH amplitude and frequency.

3.3. Frequency Variation

The average value of BJD for each segment served as the x-axis for plotting, yielding curves depicting NSH frequency and amplitude variations over time. The frequencies of NSHs were

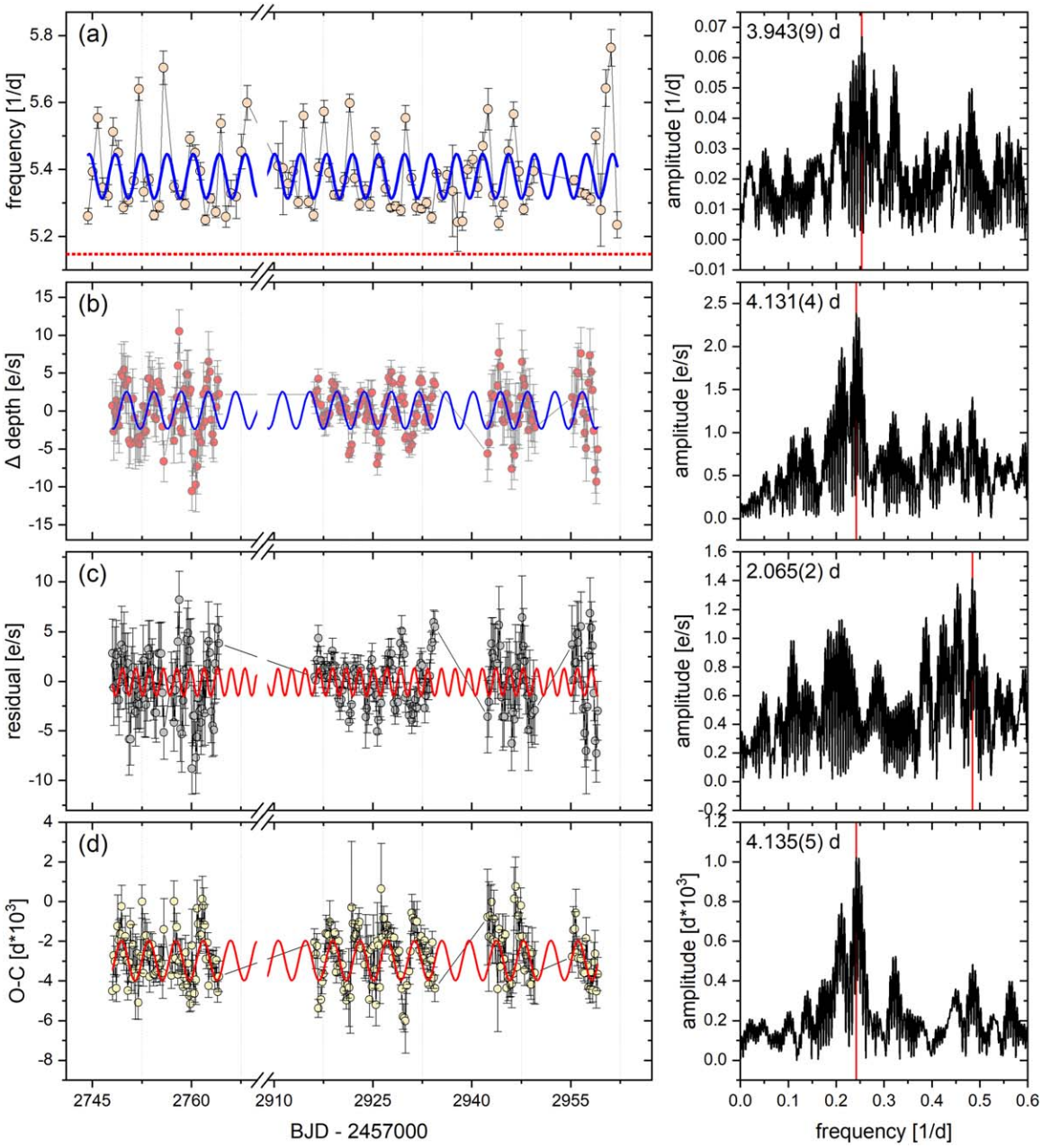

Figure 4. Frequency analysis of different curves of HS 2325+8205. Right panels: frequency spectra of the different curves; the peak frequencies have been marked using red vertical lines. Left panels: the scattered dots are the different curves, and the solid line is the sinusoidal fit corresponding to the peak frequencies (see Table 2 for parameters). (a), (b), (c), and (d) are in turn the NSH frequencies, the eclipse depths, the residuals from the fitting of the (b) panels, and $O-C$ between the observed and calculated eclipse minimum epochs. The red horizontal dashed line in (a) is the orbital frequency.

consistently higher than the orbital frequency, exhibiting periodic instabilities and variations (see Figure 4(a)). Analysis conducted using Period04 revealed that NSH frequencies exhibit periodic variations with a period of 3.943(9) days (see Figure 4(a) and Table 2). The sinusoidal fits corresponding to the peak NSH frequency are represented by blue solid lines in Figure 4(a) (Period04 software integrates frequency analysis with sinusoidal fitting; details are given in P. Lenz & M. Breger 2005).

To visualize these periodic variations more intuitively, we selected the light curve from Sector 59 as an example and zoomed in (see Figure 5). Using BJD 2459760.6121 as the zero-phase point (which was standardized for all subsequent folding), the NSH frequency changes were folded over phases 0–2, revealing the periodic changes in NSH frequency (see Figure 8(a)). This study marks the first observation of periodic variations in NSH frequencies resembling the theoretical cycle of tilted disk precession, providing crucial observational evidence for understanding the origin of NSHs.

3.4. Amplitude Variation

We have observed periodic variations in the NSH amplitude similar to the tilted disk precession period in NLs (e.g., SDSS J0812; Q.-B. Sun et al. 2023b) and IPs (e.g., TV Col; Q.-B. Sun et al. 2024a). To verify the generality of this phenomenon, we conducted a similar analysis of NSH amplitude in the DN HS 2325+8205. The NSH amplitudes

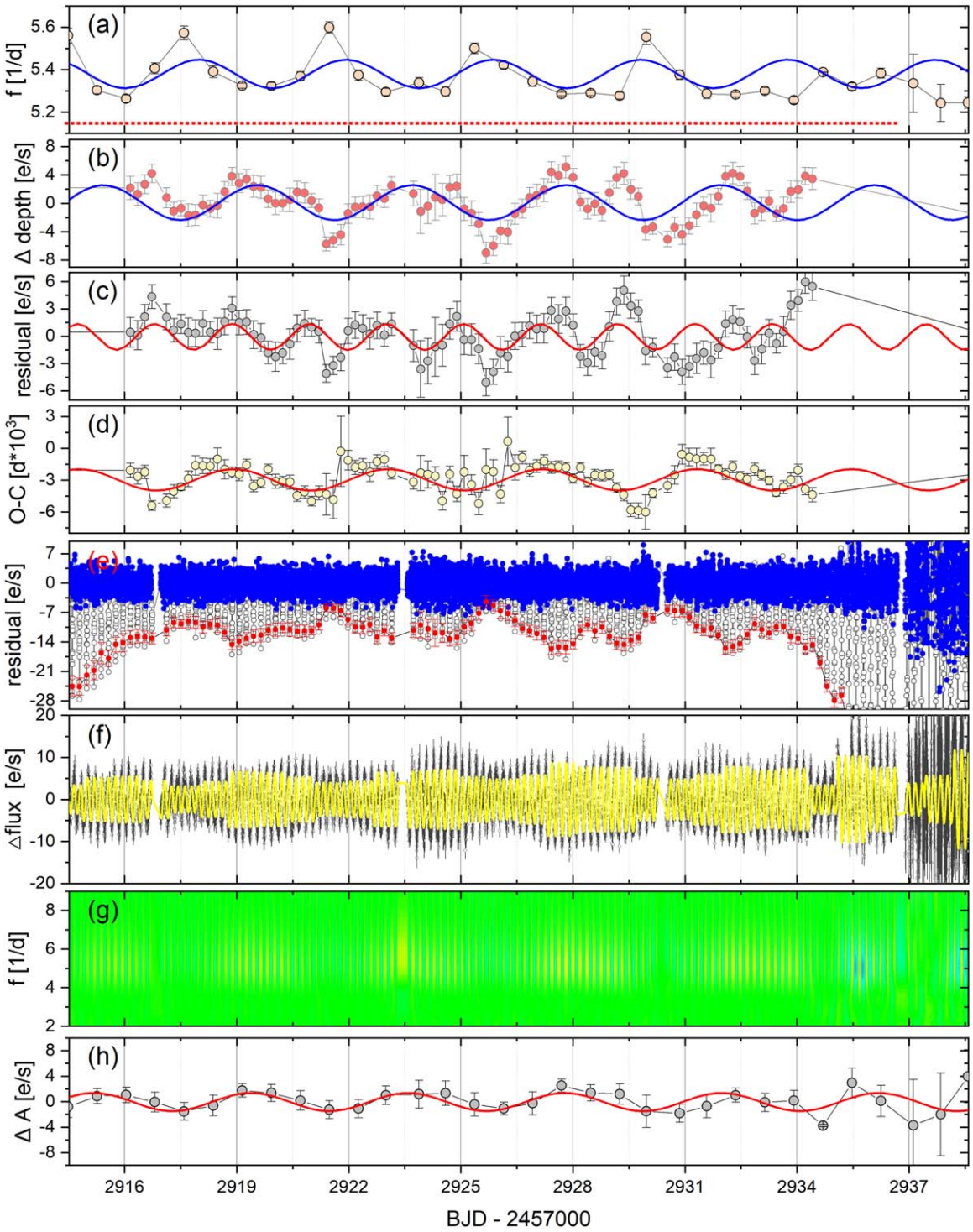

Figure 5. Details of different curves and their contrasts. The data were selected from Sector 59 in order to clearly show the details of the changes and to compare the different curves. (a) The frequency variation of NSHs is consistent with Figure 4(a). (b) The variation curve of eclipse depth is in accordance with Figure 4(b). (c) In agreement with Figure 4(c). (d) The $O-C$ variation curve is in agreement with Figure 4(d). (e) The LC#3 light curve. (f) The LC#4 light curve. (g) The CWT 2D power spectra of LC#4 are consistent with Figure 6(d). (h) The variation curve of the amplitude of NSHs is in agreement with Figure 6(b).

obtained from segmented fits exhibited both positive and negative values, with absolute values used for analysis. The analysis of NSH amplitude revealed instability characterized by various types of variations:

(a) Quadratic variation in NSH amplitude in Sector 53 (see Figure 6(a)).

(b) Long-term increase in NSH amplitude observed in Sectors 59 and 60 (see Figure 6(a)).

(c) Periodic variations in amplitude across Sectors 53, 59, and 60 (see Figure 6(b)).

(d) Amplitude of periodic variations in NSH amplitude increasing in Sectors 59 and 60 over time (see Figures 6(a) and (b)).

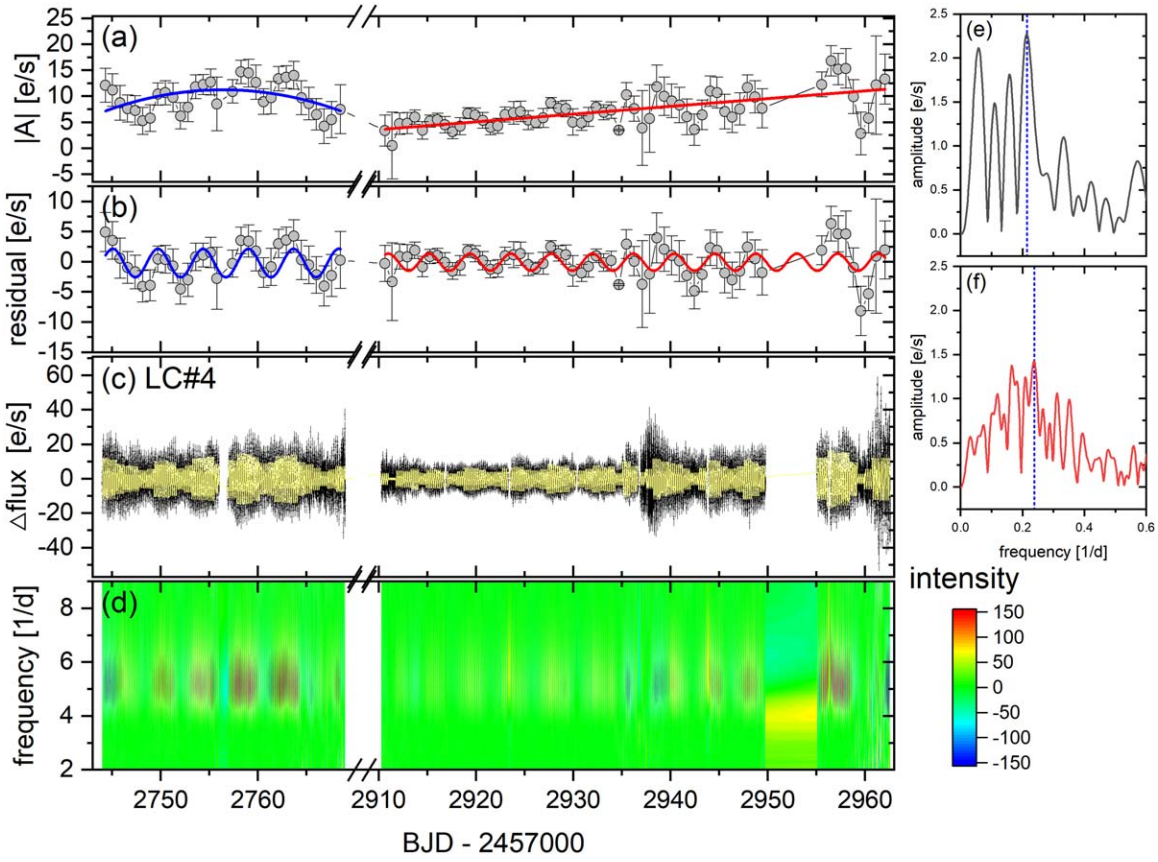

Figure 6. Analysis of the amplitudes of NSHs. (a) NSH amplitude variation curves; blue and red lines are parabolic and linear fits, respectively. (b) Residuals of the fit in layout (a); blue and red lines correspond to sinusoidal fits to the peak frequencies of the frequency analysis of the NSH amplitudes in Sector 53 and in Sectors 59 and 60, respectively. (c) Out-of-eclipse curves of LC#2 with the parabolic component removed from the segmental fit; the yellow solid line is the sinusoidal part of the segmental fit. (d) CWT 2D power spectrum of LC#4. (e) and (f) Results of the frequency analyses of the NSH amplitudes in Sector 53 and in Sectors 59 and 60, corresponding to the black and red solid lines, respectively, with the peak frequencies marked by vertical dashed lines.

To determine the period of periodic amplitude variation, we performed a parabolic fit to NSH amplitude data in Sector 53 and a linear fit in Sectors 59 and 60 (blue and red solid lines in Figure 6(a)) to mitigate long-term variations. The residual data from these fits were separately analyzed for frequency (see Figures 6(e) and (f)). The periods of amplitude variation were found to be $P_{|A|,s53} = 4.652(109)$ days and $P_{|A|,s59,s60} = 4.201(55)$ days (see Table 2). The period of Sector 53 is slightly longer than the theoretical precession period, while Sectors 59 and 60 exhibit variations closer to the theoretical precession period, a bias that may be related to the small number of data points in Sector 53.

Consistent with the approach of Q.-B. Sun et al. (2024a), we employed continuous wavelet transform (CWT; C. E. Heil & D. F. Walnut 1989) to validate changes in NSH amplitude. The segmented fitting of the out-of-eclipse curve of LC#2 provided the parabolic and sinusoidal components, yielding LC#4 after removing the quadratic component (dotted line in Figure 6(c)) and retaining only the sinusoidal component (red solid line in Figure 6(c)). CWT applied to LC#4 confirmed long-term and periodic variations in NSH amplitude. The colors of the stripes in the 2D power spectrum of CWT indicate NSH intensity. Focusing on Sector 59 (2910.2667–2936.6888, BJD–2457000), combined with Figures 6(a), (b), and (c), significant enhancement in NSH intensity and clear periodic variation in NSH amplitude were observed, consistent with segmental fitting results.

This study represents the first observation of periodic variations in NSH amplitude similar to the tilted disk precession period in DNe, underscoring the general applicability of this phenomenon.

3.5. O − C

The $O - C$ method of eclipse minima provides an effective means to study the evolution of binary star systems. In CVs, primary stars, including white dwarfs, accretion disks, and hot spots, are eclipsed by secondary stars when the orbital inclination exceeds a critical threshold. The luminosity of white dwarfs remains stable, with variations primarily attributed to the accretion disk. Eclipse minima represent the centers of brightness during these eclipses. Recent studies have indicated that eclipse minima in CVs exhibit variations similar to timescales associated with accretion disk precession. Therefore, $O - C$ analysis of eclipse minima serves as an ideal method to investigate accretion disk variations in eclipsed CVs.

Previously, we utilized the LOWESS and segmented fitting methods to remove outburst and NSH trends, resulting in LC#3 (see Figure 3(c)). Consistent with Q.-B. Sun et al. (2023b), we computed 356 eclipse minima for HS 2325+8205 using a linear superposition Gaussian fit (see Table A2). An $O - C$ analysis of these quiescent minima was carried out on the basis of an ephemeris derived from Q.-B. Sun et al.

(2023c),

$$\mathrm{Min.I} = \mathrm{BJD2458793.6762(6)} + 0.19433475(6) \times E, \quad (2)$$

where E represents the cycle number. The $O-C$ analysis revealed significant periodic variations, with frequency analysis determining periods and amplitudes of 4.135(5) days and 87.3 (89) s, respectively (see the spectrum in Figure 4 and the sinusoidal fit to peak frequency in Table 2), consistent with theoretical accretion disk precession periods. Further observation showed that the $O-C$ variation is nonsinusoidal, with a rise time approximately half that of the decline (see Figures 4(c) and 5(d)). The folded $O-C$ curve is depicted in Figure 8(e), where instead of a sinusoidal fit, we binned the curve at 0.03 phase intervals, further revealing that the $O-C$ curve rises faster than it declines.

3.6. Eclipse Depth

Using a method consistent with Q.-B. Sun et al. (2023b, 2024a), we computed the variation in eclipse depth for HS 2325+8205, utilizing the −0.5 to −0.1 and 0.1–0.5 phases of each eclipse from the LC#3 light curves as out-of-eclipse data. To exclude outburst effects, we focused on data during quiescence and performed linear fits to the eclipse depths for Sectors 53, 59, and 66, yielding the final relative eclipse depth variation curves (see Figure 4(b)). Frequency analysis of these eclipse depths revealed a periodic variation with a peak frequency of 0.2421(3) day^{-1} ($P_1 = 4.131(4)$ days). The sinusoidal fit corresponding to this peak frequency is depicted as blue solid lines in Figures 4(b) and 5(b). Further frequency analysis of residuals from the sinusoidal fit identified a periodic variation with a period of $P_2 = 2.065(2)$ days, approximately half that of P_1 (see Figures 4(c) and 5(c)).

Additionally, following Q.-B. Sun et al. (2024a), we folded the eclipse depth curve and applied both double-sine and single-sine fits. The results confirmed the presence of a biperiodic variation in the eclipse depth (see Figures 8(c) and (d)). Upon detailed comparison of the variations in LC#3 and the eclipse depth curves, the clear bipeak structure is evident in the minima (see Figures 5(b) and (e)).

This discovery represents the first observation of a biperiodic variation in eclipse depth in nonmagnetic CVs, providing crucial observational evidence for understanding tilted disk precession in CVs.

3.7. QPOs

In recent work, QPOs were identified with frequencies of 40.263(5) day^{-1} (∼2145.89 s, 1827.1297–1827.9867) and 39.871(3) day^{-1} (∼2166.99 s, 1994.2584–1995.6320) during the peak of two long outbursts in HS 2325+8205 (Q.-B. Sun et al. 2023c). In this study, QPOs were similarly detected at the peak of a long outburst in Sector 60. Following the methodology of Q.-B. Sun et al. (2023c), the top curve was selected to remove the orbital trend using a LOWESS fit (see Figure 7(a)), and frequency analysis of the residuals identified the period of the QPOs as 39.477(24) day^{-1} (∼2188.62 s, 2961.2563–2962.5730), generally consistent with previous observations (see Figure 7). Spectrograms of the three data sets were plotted to compare the three QPOs, showing no significant changes over the maximum time span of QPO detection (see Figures 7(c), (d), (e) and (g)), approximately 1135 days (∼3 yr). This stable period of QPOs in HS 2325 +8205 suggest that QPOs may have originated from physical changes on timescales longer than at least ∼3 yr, providing important observational evidence for studying the origin and characteristics of QPOs.

In addition, a comparison of the three periodograms reveals not only the presence of QPOs but also two distinct signals at frequencies of approximately 30 day^{-1} and 45 day^{-1}. The periodogram from the interval 1994.2584–1995.6320 is the most significant among them (see Figure 7(d)). Using Figure 7(d) as an example, these signals are identified as $f_1 = 29.784(56)\ \mathrm{day}^{-1}$ and $f_2 = 45.176(70)\ \mathrm{day}^{-1}$. These signals might arise from the combined frequencies of the orbital frequencies and QPOs, $f_1 \approx (39.871(3) - 2 * f_{\mathrm{orb}})\ \mathrm{day}^{-1}$ and $f_2 \approx (39.871(3) + f_{\mathrm{orb}})\ \mathrm{day}^{-1}$. The combined frequencies are still interesting to study, and the reasons why $2 * f_{\mathrm{orb}}$ and $+ f_{\mathrm{orb}}$ are observed rather than other combinations need to be explored further.

4. Discussion

4.1. Correlation of Different Windows

We observed that the NSH frequency, NSH amplitude, eclipse minima, and eclipse depth exhibit cyclic variations similar to the theoretical period of tilted disk precession. These findings suggest that although there are no SORs, the tilted disk precession is still present, and the question of why the SORs are not significant is still to be answered.

In this section, we explore their interrelationships and intrinsic significance. In Section 3.2, NSH information was derived via segmented fitting, yielding 91 data points. To enhance our analysis, $O-C$ and eclipse depth evaluations were extended to encompass 227 points during the quiescent state. Direct comparison between NSH information and $O-C$ or eclipse depth was not feasible. To proceed, we initially focused on quiescent NSH data and employed linear interpolation using eclipse minima as the base BJD to expand the data points for NSH frequency and NSH amplitude to 227 points. This method generated frequency and amplitude change curves for NSHs corresponding to each eclipse minima. Comparison between interpolated results and original curves is depicted in Figures 9(g) and (h), demonstrating consistent trends.

Figure 9 illustrates the relationships among the four variation curves. A significant correlation is evident between NSH frequency, NSH amplitude, and eclipse depth, whereas $O-C$ shows no significant relationship with the other variables. Linear fitting results reveal the following:

(a) NSH amplitude decreases as NSH frequency increases (see Figure 9(c)), confirming the opposite evolutionary trend between the two variables observed in Figures 9(g) and (h).
(b) Similarly, eclipse depth decreases with increasing NSH frequency (see Figure 9(b)), displaying notable changes as shown in Figures 5(a) and (b), with sinusoidal curves demonstrating opposite evolutionary trends.
(c) Conversely, eclipse depth increases with NSH amplitude (see Figures 9(f) and 5(b) and (h)), providing further evidence for (a) and (b) (where both NSH amplitude and eclipse depth decrease with frequency, suggesting isotropic evolution of NSH amplitude and eclipse depth).

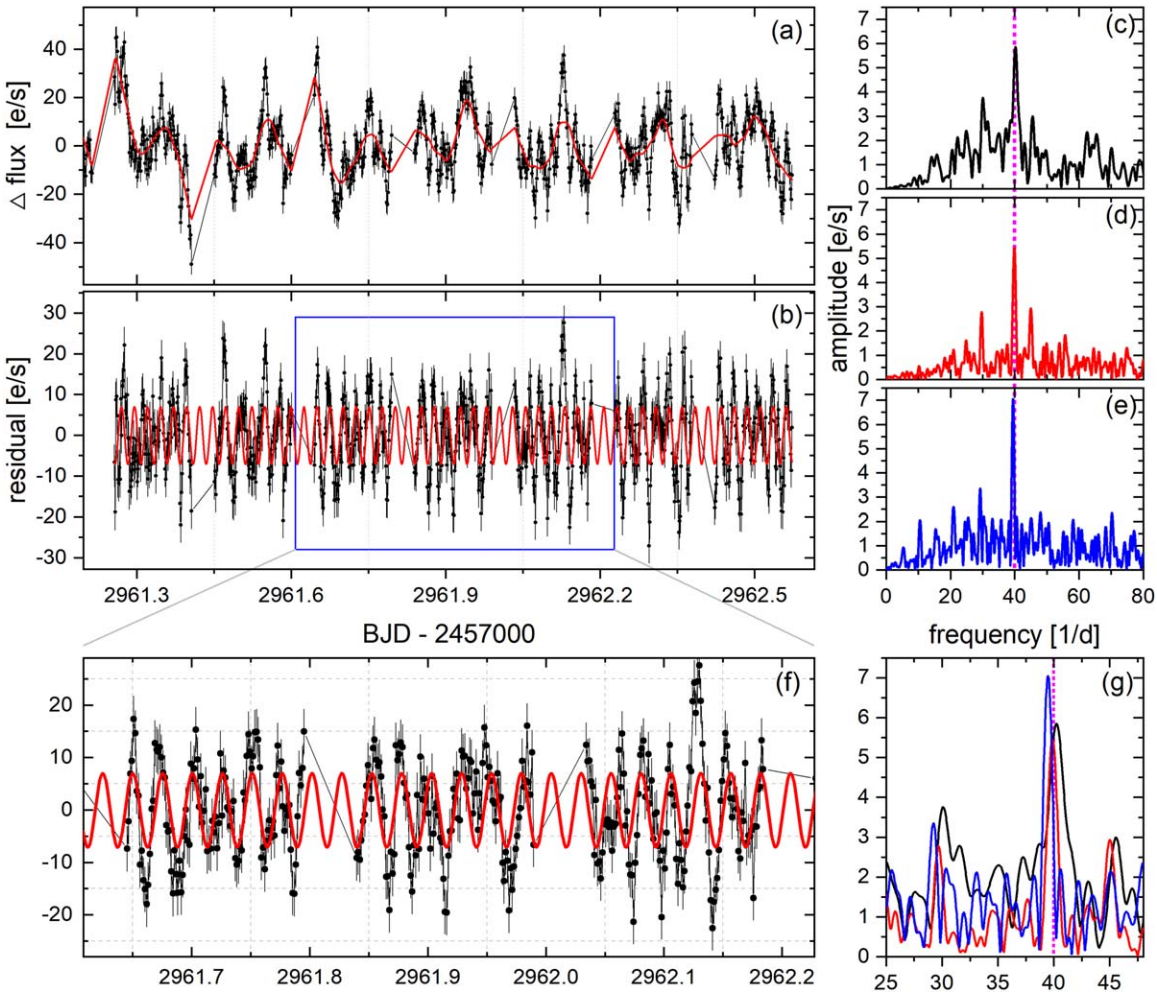

Figure 7. QPOs for HS 2325+8205 in Sector 60. (a) Outburst top of Sector 60 corresponding to the LC#3 curve; the red solid line is the LOWESS fit. (b) Residuals of the LOWESS fit; the red solid line is the sinusoidal fit corresponding to the peak frequency. (c), (d), and (e) Comparisons of the spectrograms of the three QPO light curves corresponding to the times in order 1827.1297–1827.9867, 1994.2584–1995.6320, and 2961.2563–2962.5730, and the magenta dashed line corresponds to a frequency of 40 day^{-1}. (f) Enlarged view of the light curves in the blue colored rectangular box in panel (b). (g) Combined view of panels (c), (d), and (e), with the curve colors corresponding to the individual panels in turn.

These findings offer crucial observational evidence for subsequent discussions on their origin and for investigating tilted disk precession and NSHs.

4.2. Complex Variations in NSH Amplitude

First, we utilize NSH amplitude variations as a starting point to explore various new phenomena. Before delving into these variations, let us revisit the origins of NSHs. Numerous studies support the notion that NSHs stem from periodic fluctuations in the energy released from streams impacting a retrogradely precessing tilted disk (e.g., J. M. Bonnet-Bidaud et al. 1985; D. Harvey et al. 1995; J. Patterson et al. 1997; J. Patterson 1999; M. A. Wood & C. J. Burke 2007; M. A. Wood et al. 2009; M. M. Montgomery 2009, 2012; E. Armstrong et al. 2013; D. M. Thomas & M. A. Wood 2015; M. Kimura et al. 2020; A. Bruch 2023b; Q.-B. Sun et al. 2024a). Because the tilted disk is slowly reversing precession, when fast binaries turn a circle, the streams from the secondary star will have the opportunity to enter the farthest point of the inner disk twice (two faces of the tilted disk), producing two humps with periods slightly less than half the orbital period; due to the large optical thickness of the disk, the observer will only be able to see a single hump during one orbit. The release of TESS data has provided a valuable opportunity to study the origin of NSHs, leading to the discovery of numerous new phenomena, which pose both challenges and opportunities for models of reverse precession of tilted disks.

In Section 3.4, we identify four variations characterizing the NSHs amplitude (see Figure 6): (a) parabolic variation, (b) long-term increase, (c) periodic variation, and (d) long-term increase in the amplitude of the periodic variation of the NSH amplitude. To explain these phenomena, we enumerate the main sources of NSH-related optical variations in CVs. The following possible variations will be considered in the subsequent discussion using the format, e.g., "Variable source: i":

(i) Thermal instability on the accretion disk leading to a luminosity rise (outburst; e.g., Y. Osaki 1996; J.-P. Lasota 2001; J. M. Hameury 2020).
(ii) Changes in the radius of the accretion disk (e.g., N. Vogt 1983; Y. Osaki 1989; B. Warner 1995) resulting in shifts in the impact point of the stream and consequent alterations in the released kinetic energy.

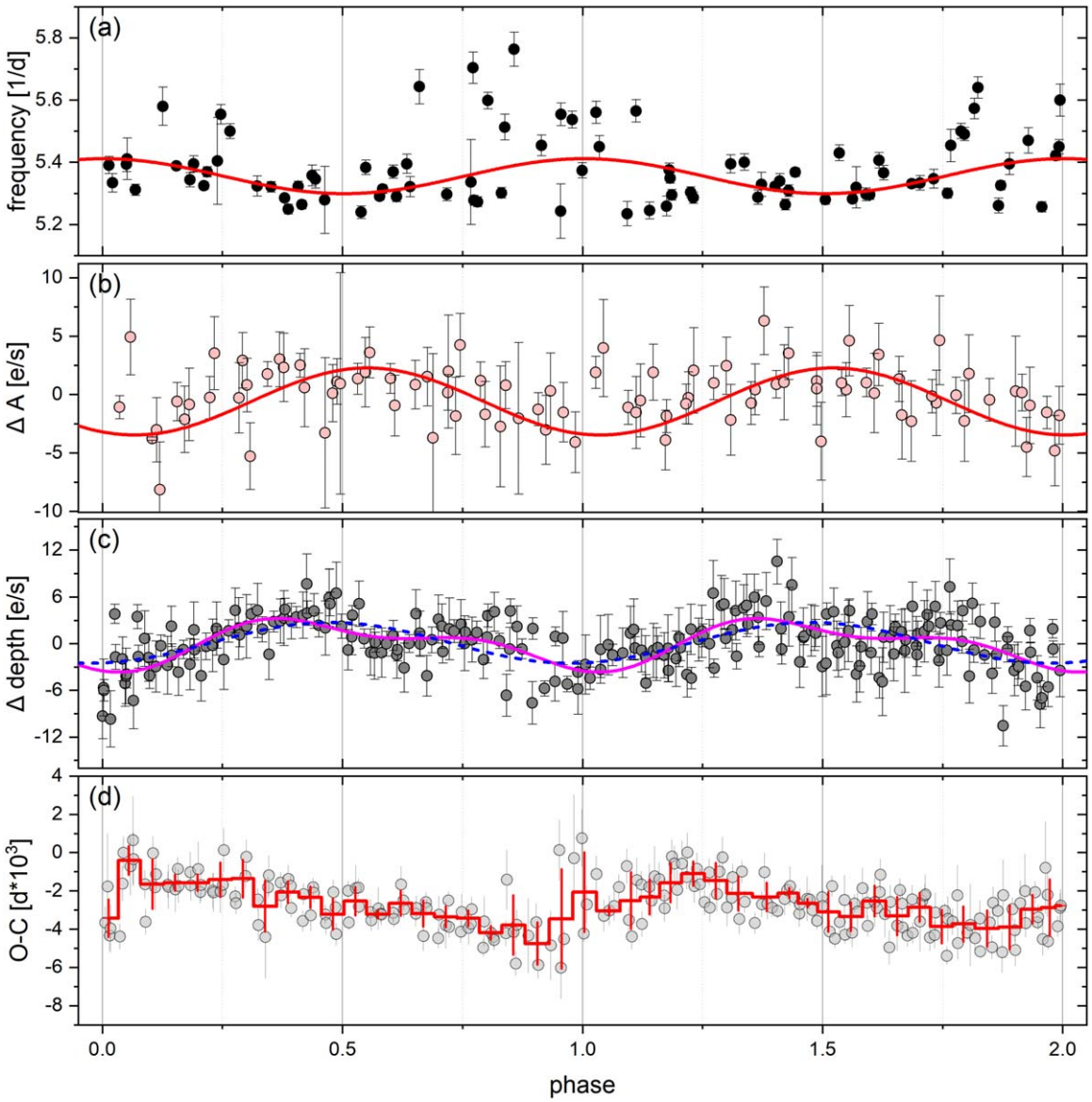

Figure 8. Different folding curves for HS 2325+8205. The zero-phase point is BJD 2459760.6121, and the folding period corresponds to the frequency analysis results of the different curves (see Table 2). (a) Folded curves for the frequency variation of the NSHs, with the red solid line being a sinusoidal fit. (b) Folded curves for the amplitude variation of the NSHs, with the red solid line being a sinusoidal fit. (c) Folded curves for the variation of the eclipse depth, with blue dashed and magenta solid lines being a single-sinusoidal and a double-sinusoidal fit, respectively. (d) Folded curves for $O - C$; the red curves are the result of binning at 0.03 phase intervals.

(iii) Variations in the matter transfer rate from the secondary star (e.g., J. Smak 2013; J. M. Hameury & J. P. Lasota 2017; J. M. Hameury 2020).
(iv) Changes in the tilt angle of the accretion disk (e.g., M. M. Montgomery 2009; Y. Osaki & T. Kato 2013; M. Kimura et al. 2020).
(v) Retrograde precession of the tilted disk, the origin of SORs.
(vi) Variation in the hot-spot position as the material stream traverses the disk, the origin of NSHs.
(vii) Variations caused by the combination of binary motion phase changes and tilted disk precession phase changes due to unchanged observational positioning.

Recent investigations have shown in DNe AH Her, ASAS J1420, TZ Per, and V392 Hya that NSH amplitudes decrease during rising outbursts and increase during declining outbursts (Q.-B. Sun et al. 2023a, 2024b), interpreted as arising from changes in the accretion disk radius (Variable source: ii). In this study, we observe a parabolic variation in NSH amplitude for HS 2325+8205 in Sector 53. Sector 53's light curve displays two incomplete outbursts at its start and end (see Figure 3(a); 2743.9942–2768.9765), with the middle period in quiescence. Additionally, NSHs in Sector 53 exhibit their highest amplitudes during quiescence, decreasing during rising outbursts and increasing during declining outbursts, mirroring the behavior observed in AH Her. Consequently, we suggest that the parabolic variation in NSH amplitude in Sector 53 stems from changes in the accretion disk radius (Variable source: ii). During outburst rise, the disk radius expands, reducing the distance from the Lagrangian L1 point to the disk contact point, thereby diminishing the energy release from the material. Conversely, during outburst decline, the disk contracts. However, the absence of significant parabolic variation in

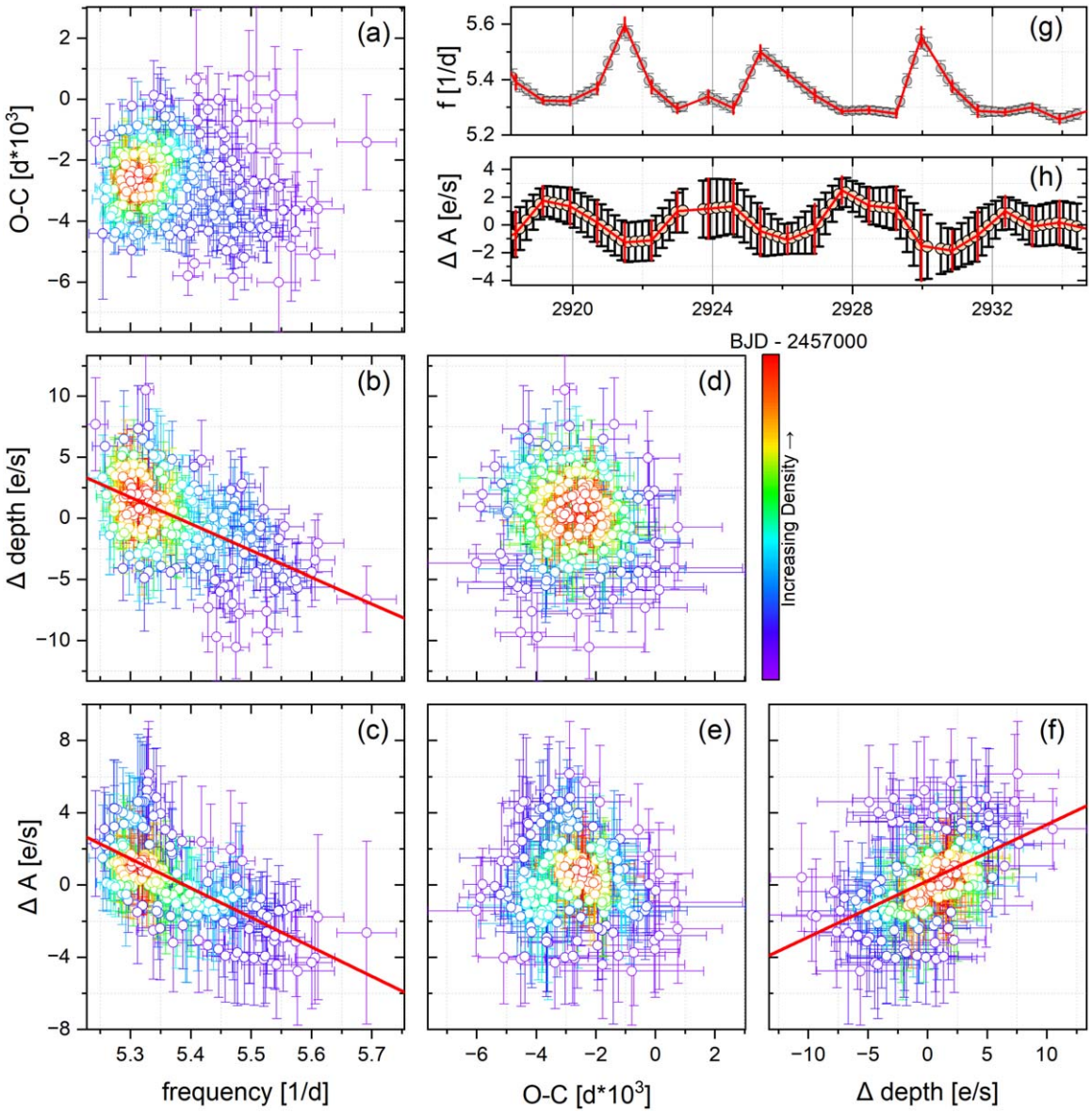

Figure 9. Correlation of different curves. (a), (b), (c), (d), (e), and (f) in order of NSH frequency vs. $O-C$, NSH frequency vs. eclipse depth, NSH frequency vs. NSH amplitude, $O-C$ vs. eclipse depth, $O-C$ vs. NSH amplitude, $O-C$ vs. NSH amplitude, and eclipse depth vs. NSH amplitude. The colors in the figure indicate the density (amount of data per unit area), with redder colors indicating more data points per unit area. (g) and (h) Examples and results of linear interpolation of NSH frequency and amplitude; the dotted line in the figure is the result of interpolation, and the red line is the raw data.

Sectors 59 and 60 is perplexing and might be obscured by longer-term, more pronounced variations.

Periodic variations in NSH amplitude have been observed in NL SDSS J0812 (Q.-B. Sun et al. 2023b) and IP TV Col (Q.-B. Sun et al. 2024a), and this phenomenon is noted for the first time in DNe. This periodic variation provides strong evidence for the presence of a tilted disk with reverse precession in NSHs. Consistent with interpretations of SDSS J0812 and TV Col, the origin of the periodic amplitude variation may be akin to the origin of SORs, stemming from the periodic variation in the apparent hot-spot area due to tilted disk precession (Variable source: vii).

Additionally, we have newly identified that the amplitude of cyclic variations in NSH amplitude increases with a long-term increase in NSH amplitude. The amplitudes of NSHs in Sectors 59 and 60 exhibit a prolonged increase beyond the outburst timescale, potentially associated with changes in the tilt angle of the disk (Variable source: iv) and the rate of matter transfer (Variable source: iii). The relationship between the orbital and NSHs and the tilted disk precession frequency can be expressed as (J. C. B. Papaloizou & C. Terquem 1995; J. Larwood 1998; Y. Osaki & T. Kato 2013; J. Smak 2013; M. Kimura et al. 2020; S. Y. Stefanov & A. K. Stefanov 2023)

$$\nu_{\rm nsh} - \nu_{\rm orb} = \nu_{\rm prec} = -\frac{3}{8\pi}\frac{GM_2}{a^3}\frac{\int \Sigma r^3 dr}{\int \Sigma \Omega r^3 dr}\cos\theta, \qquad (3)$$

where $\nu_{\rm nsh}$ is the orbital frequency, $\nu_{\rm orb}$ is the NSH frequency, $\nu_{\rm prec}$ is the tilted disk precession frequency, G is the gravitational constant, M_2 is the mass of the secondary, a is the binary separation, Σ is the surface density of the disk, Ω is the Keplerian angular velocity of the disk matter, r is the radial distance from the accretion disk to the white dwarf, and θ is the tilt angle. Assuming the other parameters are constant, an

increase in the tilt angle leads to an increase in $\nu_{\rm nsh}$, but our analysis of NSH frequencies reveals no significant long-term increasing trend except for periodic variations. Hence, as noted by J. Smak (2013), this may be related to a long-term increase in the matter transfer rate (Variable source: iii). If there is a sustained increase in the material transfer rate, this could also explain the long-term increase in the amplitude of periodic NSH amplitude variations, which are larger for the same orbital phase and tilted disk precession phase.

4.3. Not Only IPs but Also DNe

Periodic variations in eclipse depth related to tilted disk precession have been observed in NL DW UMa (D. R. S. Boyd et al. 2017) and NL variables (Iłkiewicz et al. 2021). In our recent studies, we have detected periodic variations in eclipse depth in both IP TV Col (Q.-B. Sun et al. 2024a) and NL SDSS J0812 (Q.-B. Sun et al. 2023b). TV Col exhibits biperiodic variations with periods $P_1 = 3.905(11)$ days and $P_2 = 1.953(4)$ days, where $P_1 \approx P_{\rm prec} \approx 2 \times P_2$. We interpreted P_1 as evidence of tilted disk precession, attributing it to periodic changes in the apparent area of the tilted disk. The occurrence of P_2 exclusively in IPs, not NLs, led us to propose that this biperiodic variation might be linked to the precession of two accretion curtains along with the tilted disk. However, this hypothesis has evolved with the findings presented in this paper.

In our recent study, we present the first evidence of biperiodic variations in eclipse depth in the DN HS 2325+8205 ($P_1 = 4.131(4)$ days, $P_2 = 2.065(2)$ days, $P_{\rm prec} = 4.171(17)$ days) resembling those observed in TV Col. Interestingly, this biperiodic variation in eclipse depth is not exclusive to IPs. The amplitude of P_1 in HS 2325+8205 is approximately twice that of P_2 (see Table 2), suggesting that P_1 originates from a brighter source compared to P_2. P_1 closely matches the theoretical precession period of the tilted disk, implying periodic changes in the brightness of the eclipsing center due to tilted disk precession, further supporting the evidence of tilted disk precession. Additionally, we found a correlation where the eclipse depth increases with the amplitude of NSHs (see Figures 9(f) and 5(b) and (h)), consistent with our interpretation of cyclic variations in NSH amplitude and eclipse depth with P_1. As the apparent area of the hot spot increases, so does the eclipse depth.

Surprising and confusing is the change in period for P_2. However, when this phenomenon was first noticed in the IP TV Col, we suggested that it was due to the accretion curtain precessing with the tilted disk (Q.-B. Sun et al. 2024a). Yet, the same variation was found in the nonmagnetic DN HS 2325 +8205, which showed no relation to the accretion curtain. P_2 is approximately half of the theoretical period of tilted disk precession, suggesting a clear association with tilted disk precession. Simply put, during one complete precession cycle of the tilted disk ($P_{\rm prec}$), the tilted disk reveals an additional bright source appearing twice, or two sources appearing once each, in addition to the brightness of the disk itself. A similar change in tilted disk precession is the fact that the stream does have the opportunity to enter the furthest point twice on two faces of the tilted disk. This implies that the additional brightness source is likely still due to the motion of the hot spot across the disk face.

Additionally, the observation that this biperiodic variation is evident in the eclipse depth but not in the NSH amplitude, NSH frequency, or $O-C$ highlights a distinct difference in the origins of these variations. To fully understand this, it is crucial to consider or rule out various possible factors, including the type of binary system, orbital inclination, fluctuations in the accretion disk's transparency, and the distribution of material, among others. Detailed studies are scarce, and additional observational evidence is necessary to validate our hypotheses. We also caution that the biperiodic variation may alternatively manifest as a bipeak variation in eclipse depth.

4.4. New Evidence for the Origin of NSHs

In Section 3.3, we identify a periodic variation in the frequency of NSHs in DN HS 2325+8205 ($P_{\rm fre} = 3.943$ (9) days), which closely matches the theoretical period of tilted disk precession, observed here for the first time. To verify this phenomenon, we try to seek validation in SDSS J0812 and TV Col. Frequency analyses were conducted using segmented fit parameters reported in Q.-B. Sun et al. (2023b, 2024a). The results reveal periodic variations in NSH frequency with periods of $P_{\rm fre} = 3.111(29)$ days ($P_{\rm prec} = 3.0451(5)$ days; Q.-B. Sun et al. 2023b) and $P_{\rm fre} = 3.913(30)$ days ($P_{\rm prec} = 3.895(5)$ days; Q.-B. Sun et al. 2024a) in SDSS J0812 and TV Col, respectively (see Figure 10). This establishes that periodic variations in NSH frequency, approximately matching the period of tilted disk precession, are common across NLs, IPs, and DNe.

The NSH frequency variation can be described by Equation (3), where the orbital and precession frequencies are pivotal. Additionally, we observe a periodic variation in the $O-C$ diagram of eclipse minima in HS 2325+8205 ($P_{O-C} = 4.135(5)$ days and $A_{O-C} = 87.3(89)$ s; see Section 3.5), characterized by a faster rise than fall. This could potentially contribute to the observed frequency variations of NSHs, given that $O-C$ variations stem from changes in the orbital period. Unfortunately, such short-term periodic $O-C$ variations cannot be attributed to dominant long-term magnetic activity cycles (J. H. Applegate 1992), the light travel time effect caused by a third body (J. B. Irwin 1952; T. Borkovits & T. Hegedüs 1996), or slight amplitude fluctuations of the accretion disk (B. E. Schaefer 2021). Instead, they likely represent periodic oscillations of the eclipse center due to accretion disk precession (E. De Miguel et al. 2016; Q.-B. Sun et al. 2023b, 2024a).

If NSH frequency variations are indeed linked to changes in the period of tilted disk precession, periodic fluctuations in the precession period would be expected. However, the SOR cycle remains stable in both SDSS J0812 and TV Col. Moreover, the possibility of alternating acceleration and deceleration within a single precession cycle of the tilted disk could potentially produce asymmetric signals in the SORs (constant SOR period but with asymmetric nonsinusoidal changes in shape). Yet no such asymmetry was detected in the nearly sinusoidal variations of the SORs observed in SDSS J0812 and TV Col. Therefore, we propose that NSH frequency variations are not solely a product of the precession cycle.

Crucial observations include $P_{\rm fre} \approx P_{\rm prec}$, the NSH amplitude decreasing with increasing NSH frequency, and the inverse correlation observed between eclipse depth and NSH frequency (see Section 4.1 and Figure 9). This suggests that if NSH frequency variation is not directly related to the tilt disk precession period, it may correlate with the precession phase. We suggest that such variations may arise from an interaction between the orbital phase and tilted disk precession phase, similar to the variations observed in NSH amplitude and eclipse

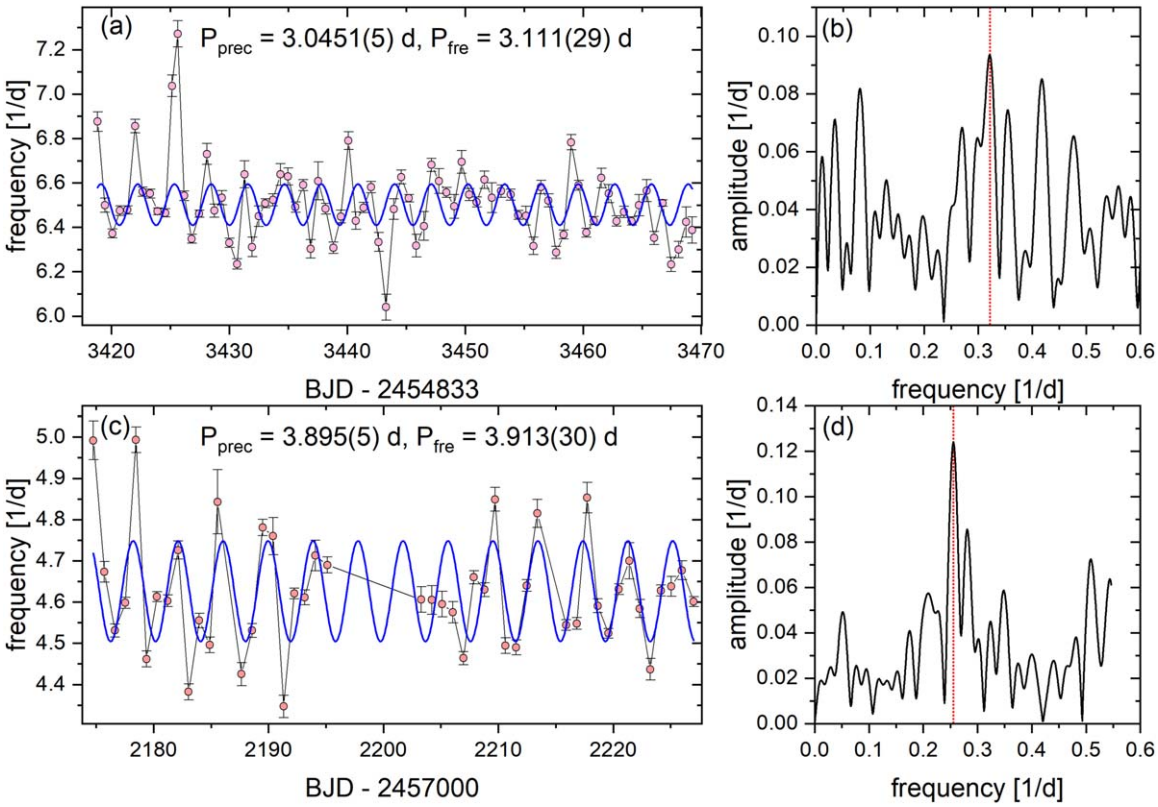

Figure 10. NSH frequency variation curves and frequency analysis of SDSS J0812 and TV Col. The data presented are sourced from Q.-B. Sun et al. (2023b) for SDSS J0812 and Q.-B. Sun et al. (2024a) for TV Col. In each subplot, the vertical solid line indicates the peak frequency, and the blue solid line represents the sinusoidal fit corresponding to this peak frequency. (a) and (b) correspond to the NSH frequency variations and corresponding frequency analyses for SDSS J0812, while (c) and (d) correspond to the NSH frequency variations and corresponding frequency analyses for TV Col.

depth. However, the exact mechanism remains puzzling and requires further study.

5. Conclusions

In this paper, we present an in-depth study of the tilted disk precession and the origin of the NSHs based on TESS photometry using an analysis similar to that of Q.-B. Sun et al. (2023b, 2024a), with a sample of the long-period eclipsing DN HS 2325+8205. We utilize the eclipsing minima $O-C$, the eclipsing depth, the NSH frequency, the NSH amplitude, and the correlation between them as the windows. The main results are as follows:

(1) For the first time, we found NSHs with periods of 0.185671(17) day ($\epsilon = -0.0445(2)$) in HS 2325+8205, but no SORs. Discontinuities in NSHs and the absence of a co-occurrence of SORs and NSHs in HS 2325+8205 provide observational evidence for studying the formation and cessation of tilted disks and NSHs. Additionally, we rediscovered QPOs with a period of ∼2188.62 s (39.477(24) day^{-1}) in the new observational data, with the period remaining stable for over 3 yr. This provides crucial observational evidence for understanding the origin of QPOs.

(2) In HS 2325+8205, a similar periodic variation in the NSH frequency ($P_{\rm fre} = 3.943(9)$ days) was found as in the tilted disk precession cycle. Subsequently, we verified this in NL SDSS J0812 ($P_{\rm fre} = 3.111(29)$ days) and IP TV Col ($P_{\rm fre} = 3.913(30)$ days) and again found similar periodic variations, suggesting that this phenomenon is general. In addition, we found that both NSH amplitude and eclipse depth decreased with increasing NSH frequency. Therefore, we suggest that the periodic variations in NSH frequency may have a similar origin to the periodic variations in NSH amplitude and eclipse depth from the interaction of the orbital phase with the tilted disk precession phase.

(3) The NSH amplitude exhibits complex variations, including (a) parabolic variation in Sector 53, (b) a long-term increase in Sectors 59 and 60, (c) periodic variation across all sectors, and (d) a long-term increase in the amplitude of the periodic variation of the NSH amplitude in Sectors 59 and 60. We suggest that (a) may resemble DNe AH Her, ASAS J1420, TZ Per, and V392 Hya, attributable to variations in the accretion disk radius; (b) may be associated with variations in the matter transfer rate; (c) mirrors the origin of SORs from cyclic variations in the hot-spot apparent area; and (d) may result from combined variations in the matter transfer rate and hot-spot apparent area.

(4) Similarly, we found periodic variations in the eclipsing minima $O-C$ of HS 2325+8205, with periods and amplitudes $P_{O-C} = 4.135(5)$ days and $A_{O-C} = 87.3(89)$ s, respectively. These variations may be linked to periodic changes in the eclipsing center in response to tilted disk precession. Additionally, we observed that the rate of rise

of $O-C$ is about half that of the rate of fall, indicating the asymmetric brightness distribution of the tilted disk.

(5) Analogous to IP TV Col, we identified biperiodic variations in eclipse depth with periods $P_1 = 4.131(4)$ days and $P_2 = 2.065(2)$ days ($P_1 \approx P_{\rm prec} \approx 2 \times P_2$) in DN HS 2325+8205. This is the first observation of such cycles in DNe, suggesting that the variation with period P_2 may not be related to the accretion curtain. We suggest that the periodic variation with period P_2 may also arise from material streams impacting the furthest points of the two sides.

We conducted a detailed study of tilted disk precession and NSHs in DN HS 2325+8205 across multiple observation windows. Our results indicate the presence of periodic variations approximately matching the precession period in $O-C$, eclipse depth, NSH frequency, and NSH amplitude. These findings strongly support the existence of tilted disk precession, although no SORs were detected, and the question of why the SORs are not significant urgently needs to be addressed. The most intricate variations observed are in NSH frequency, NSH amplitude, and eclipse depth, and there is a correlation between them. This paper provides important observational evidence on these phenomena, which is key evidence for the study of the origin of the NSHs.

Acknowledgments

This work was supported by the National Key R&D Program of China (grant No. 2022YFE0116800) and the National Natural Science Foundation of China (grant No. 11933008). In the compilation of this paper, we have relied heavily on the invaluable data gathered by the TESS survey, and we express our heartfelt appreciation to all the diligent personnel involved in this esteemed mission. Additionally, we recognize with gratitude the Mikulski Archive for Space Telescopes (MAST) at the Space Telescope Science Institute for hosting and facilitating access to all the data presented herein. All of the TESS data used in this paper can be found through MAST: doi:10.17909/6xrj-6k75.

Appendix
Supplementary Material

This appendix contains Tables A1 and A2. Table A1 shows the segmented parabolic superimposed sinusoidal fitting parameters, calculated as described in Section 3.2 of the main paper. Table A2 shows the quiescent eclipsing parameters for HS 2325+8205, including eclipsing minima, depth, E, and $O-C$ analyses.

Table A1
Parameters Obtained from Fitting the NSHs Using a Parabolic Superimposed Sine Fit

Start[a] (BJD)	End[a] (BJD)	During (day)	Z (e s^{-1})	Err. (e s^{-1})	B (e (s day)$^{-1}$)	Errors (e (s day^2)$^{-1}$)	C (e (s day^2)$^{-1}$)	Errors (e (s day^2)$^{-1}$)	A (e s^{-1})	Errors (e s^{-1})	Freq. (1 day^{-1})	Errors (1 day^{-1})	p (rad)	Errors (rad)	ν[b]	$\chi^2_{\rm red}$[c]
2743.9942	2744.6484	0.65	35.43	3.93	−1.94E+05	2.16E+04	2.67E+08	2.96E+07	12.105	3.235	5.261	0.024	350.46	64.92	368	21.29
2744.6498	2745.4262	0.78	2.88	0.98	−1.58E+04	5.40E+03	2.17E+07	7.41E+06	11.185	3.117	5.393	0.023	−13.41	63.79	433	23.92
2745.4275	2746.2026	0.78	−12.73	0.77	6.99E+04	4.21E+03	−9.60E+07	5.78E+06	8.710	3.334	5.554	0.032	−454.19	87.24	429	26.19
2746.2039	2746.9803	0.78	−3.70	1.89	2.03E+04	1.04E+04	−2.79E+07	1.43E+07	7.616	2.603	5.346	0.029	117.15	79.85	430	18.51
2746.9817	2747.7581	0.78	5.16	0.90	−2.83E+04	4.93E+03	3.89E+07	6.78E+06	7.286	2.789	5.321	0.032	184.07	89.08	432	16.62
2747.7595	2748.5345	0.78	3.30	0.94	−1.81E+04	5.15E+03	2.49E+07	7.07E+06	5.258	2.598	5.513	0.042	−340.81	114.47	429	17.87
2748.5359	2749.3123	0.78	3.40	1.33	−1.87E+04	7.34E+03	2.57E+07	1.01E+07	5.779	2.554	5.450	0.036	−168.24	99.56	430	13.41
2749.3137	2750.0901	0.78	2.16	1.41	−1.19E+04	7.75E+03	1.63E+07	1.07E+07	10.423	2.167	5.286	0.018	281.54	49.86	426	15.14
2750.0915	2750.8665	0.78	0.08	1.42	−4.56E+02	7.81E+03	6.28E+05	1.07E+07	10.677	2.322	5.308	0.019	219.90	51.43	428	15.34
2750.8679	2751.6443	0.78	9.32	0.86	−5.13E+04	5.06E+03	7.06E+07	3.04E+06	9.784	2.797	5.366	0.024	60.75	65.19	431	16.44
2751.6457	2752.4207	0.78	4.58	0.90	−2.52E+04	5.23E+03	3.47E+07	3.41E+06	6.215	2.531	5.640	0.034	−692.07	94.10	431	17.06
2752.4221	2753.1985	0.78	13.97	0.43	−7.69E+04	2.37E+03	1.06E+08	3.26E+06	7.865	2.758	5.334	0.029	150.08	80.97	430	15.99
2753.1999	2753.9763	0.78	7.61	0.86	−4.19E+04	3.15E+03	5.77E+07	1.21E+07	11.828	2.287	5.369	0.016	54.06	44.78	431	14.76
2753.9776	2754.7527	0.78	−5.78	1.27	3.19E+04	7.02E+03	−4.39E+07	9.66E+06	12.233	1.951	5.263	0.014	343.29	38.32	430	12.31
2754.7540	2755.5304	0.78	3.57	1.27	−1.97E+04	7.00E+03	2.71E+07	9.65E+06	12.719	2.512	5.289	0.017	272.98	46.57	430	14.71
2755.5318	2755.9930	0.46	95.65	0.68	−5.27E+05	5.29E+03	7.26E+08	7.29E+06	8.496	5.167	5.704	0.050	−868.25	138.76	265	17.73
2756.9124	2757.8624	0.95	7.64	0.96	−4.21E+04	5.29E+03	5.81E+07	7.29E+06	10.921	2.236	5.349	0.017	108.17	46.94	524	21.33
2757.8638	2758.6402	0.78	−1.83	0.85	1.01E+04	4.66E+03	−1.39E+07	6.43E+06	14.675	2.231	5.323	0.013	181.60	35.84	433	15.97
2758.6416	2759.4166	0.78	−3.32	0.68	1.83E+04	3.78E+03	−2.53E+07	5.21E+06	14.474	2.665	5.296	0.016	254.99	43.47	429	18.96
2759.4180	2760.1944	0.78	−1.67	0.72	9.19E+03	4.00E+03	−1.27E+07	5.51E+06	12.693	3.322	5.490	0.021	−281.49	58.67	430	22.68
2760.1958	2760.9722	0.78	11.45	1.08	−6.32E+04	5.96E+03	8.72E+07	8.23E+06	8.969	2.471	5.450	0.023	−169.72	63.74	433	17.39
2760.9736	2761.7486	0.78	−0.98	1.41	5.39E+03	7.79E+03	−7.44E+06	1.07E+07	9.717	3.105	5.395	0.026	−17.28	71.93	429	19.51
2761.7500	2762.5264	0.78	−9.63	1.22	5.32E+04	6.72E+03	−7.34E+07	9.28E+06	13.346	2.338	5.249	0.015	386.13	42.07	430	16.80
2762.5278	2763.3028	0.78	7.80	1.46	−4.31E+04	8.07E+03	5.95E+07	1.11E+07	13.671	2.167	5.314	0.014	206.96	37.37	424	14.43
2763.3042	2764.0806	0.78	−5.09	0.74	2.82E+04	4.07E+03	−3.89E+07	5.63E+06	14.025	2.676	5.273	0.016	319.25	45.33	429	18.47
2764.0820	2764.8584	0.78	−16.19	2.34	8.95E+04	1.29E+04	−1.24E+08	1.79E+07	9.739	3.260	5.537	0.027	−411.05	75.27	431	23.17
2764.8598	2765.6348	0.78	−3.95	0.51	2.18E+04	2.85E+03	−3.02E+07	3.94E+06	8.566	3.131	5.259	0.032	360.21	87.47	430	28.91
2765.6362	2766.4126	0.78	−86.57	0.43	4.79E+05	2.37E+03	−6.62E+08	3.28E+06	6.508	3.029	5.329	0.039	165.12	108.17	430	22.89
2766.4140	2767.1904	0.78	−127.30	0.49	7.04E+05	2.72E+03	−9.75E+08	3.77E+06	4.239	3.334	5.319	0.066	191.87	182.82	432	26.90
2767.1918	2767.9668	0.78	−29.87	0.45	1.65E+05	2.47E+03	−2.29E+08	3.42E+06	5.507	3.459	5.454	0.052	−180.49	144.06	429	30.67
2767.9682	2768.9765	1.01	44.98	14.80	−2.49E+05	8.19E+04	3.45E+08	1.13E+08	−7.484	4.711	5.599	0.052	−584.12	142.82	566	74.14
2910.2667	2910.9890	0.72	33.58	4.33	−1.95E+05	2.52E+04	2.84E+08	3.67E+07	3.397	3.014	5.411	0.067	−65.36	195.02	392	16.10
2910.9903	2911.7667	0.78	−7.28	0.21	4.24E+04	1.19E+03	−6.17E+07	1.74E+06	−0.495	6.432	5.404	0.139	1.51	1.75	430	10.84
2911.7681	2912.5445	0.78	−14.18	0.60	8.26E+04	3.50E+03	−1.20E+08	5.09E+06	4.749	2.082	5.357	0.033	90.38	96.50	430	9.30
2912.5459	2913.3209	0.78	−9.50	0.27	5.54E+04	1.59E+03	−8.06E+07	2.32E+06	−4.818	2.020	5.395	0.031	−19.64	89.85	432	7.32
2913.3223	2914.0987	0.78	8.59	0.85	−5.01E+04	4.94E+03	7.29E+07	7.20E+06	6.025	1.367	5.302	0.017	252.84	50.87	430	5.00
2914.1001	2914.8765	0.78	−2.03	0.31	1.18E+04	1.82E+03	−1.73E+07	2.65E+06	3.445	1.699	5.560	0.036	−500.76	104.59	430	4.77
2914.8778	2915.6528	0.78	1.02	0.31	−5.93E+03	1.80E+03	8.64E+06	2.62E+06	5.227	1.172	5.303	0.017	248.86	50.19	431	3.73
2915.6542	2916.4306	0.78	−6.30	0.97	3.67E+04	5.67E+03	−5.36E+07	8.27E+06	5.509	1.227	5.264	0.017	363.77	50.64	429	3.64
2916.4320	2917.2084	0.78	2.52	0.60	−1.47E+04	3.51E+03	2.14E+07	5.12E+06	4.522	1.560	5.406	0.025	−52.13	73.39	314	3.58
2917.2098	2917.9848	0.78	10.32	0.22	−6.02E+04	1.28E+03	8.79E+07	1.87E+06	3.174	1.389	5.573	0.033	−538.11	96.08	429	4.18
2917.9862	2918.7626	0.78	10.74	0.31	−6.27E+04	1.79E+03	9.15E+07	2.61E+06	4.222	1.635	5.391	0.028	−6.22	80.50	429	4.24
2918.7640	2919.5403	0.78	−2.05	0.77	1.20E+04	4.51E+03	−1.75E+07	6.59E+06	6.696	1.054	5.324	0.012	187.15	34.97	430	2.91
2919.5417	2920.3167	0.78	4.29	0.27	−2.51E+04	1.56E+03	3.66E+07	2.28E+06	6.405	1.335	5.323	0.016	191.98	46.31	431	3.85
2920.3181	2921.0945	0.78	6.11	0.33	−3.57E+04	1.94E+03	5.21E+07	2.83E+06	5.351	1.529	5.369	0.021	55.26	61.37	430	3.65
2921.0959	2921.8709	0.78	4.56	0.45	−2.67E+04	2.65E+03	3.90E+07	3.87E+06	4.019	1.414	5.598	0.026	−612.74	77.18	430	4.23
2921.8723	2922.6487	0.78	4.34	0.39	−2.54E+04	2.31E+03	3.71E+07	3.37E+06	4.302	1.447	5.374	0.025	42.98	72.17	432	3.27
2922.6501	2923.3195	0.67	1.53	0.26	−8.92E+03	1.53E+03	1.30E+07	2.24E+06	6.514	1.440	5.295	0.017	273.82	49.53	384	3.83
2923.5653	2924.2028	0.64	5.42	0.33	−3.17E+04	1.96E+03	4.63E+07	2.86E+06	6.810	2.166	5.339	0.024	143.76	70.51	357	6.48
2924.2042	2924.9806	0.78	0.53	0.65	−3.08E+03	3.81E+03	4.49E+06	5.58E+06	7.077	1.936	5.297	0.021	266.98	60.83	432	6.57
2924.9820	2925.7584	0.78	−1.71	0.34	1.00E+04	2.00E+03	−1.46E+07	2.93E+06	5.414	1.825	5.500	0.025	−326.80	72.30	430	6.33
2925.7598	2926.5348	0.78	−0.74	0.19	4.34E+03	1.12E+03	−6.36E+06	1.64E+06	4.905	0.990	5.421	0.016	−94.92	45.41	430	3.18
2926.5361	2927.3125	0.78	7.95	0.34	−4.66E+04	1.97E+03	6.81E+07	2.88E+06	5.831	1.804	5.344	0.023	131.26	67.10	431	5.67

Table A1
(Continued)

Start[a] (BJD)	End[a] (BJD)	During (day)	Z (e s^{-1})	Err. (e s^{-1})	B (e (s day)$^{-1}$)	Errors (e (s day^2)$^{-1}$)	C (e (s day^2)$^{-1}$)	Errors (e (s day^2)$^{-1}$)	A (e s^{-1})	Errors (e s^{-1})	Freq. (1 day^{-1})	Errors (1 day^{-1})	p (rad)	Errors (rad)	ν[b]	$\chi^2_{\rm red}$[c]
2927.3139	2928.0903	0.78	−0.80	0.54	4.69E+03	3.17E+03	−6.87E+06	4.63E+06	8.719	1.018	5.285	0.009	301.63	26.16	430	2.78
2928.0917	2928.8667	0.77	−6.11	0.46	3.58E+04	2.72E+03	−5.24E+07	3.98E+06	7.710	1.268	5.290	0.013	286.94	36.83	431	3.66
2928.8681	2929.6444	0.78	−0.63	0.38	3.68E+03	2.21E+03	−5.40E+06	3.24E+06	7.631	1.589	5.278	0.016	324.65	46.56	431	4.37
2929.6458	2930.2792	0.63	22.78	1.03	−1.33E+05	6.03E+03	1.96E+08	8.84E+06	5.040	2.533	5.554	0.037	−484.99	107.12	358	6.42
2930.4958	2931.1986	0.70	8.97	0.42	−5.26E+04	2.44E+03	7.70E+07	3.58E+06	4.844	1.414	5.375	0.022	38.94	63.30	379	3.07
2931.2000	2931.9764	0.78	3.44	0.63	−2.02E+04	3.67E+03	2.96E+07	5.38E+06	6.057	1.822	5.287	0.023	297.39	66.64	431	6.08
2931.9778	2932.7541	0.78	−1.10	0.58	6.43E+03	3.40E+03	−9.43E+06	4.98E+06	7.908	1.108	5.282	0.011	311.60	31.38	430	3.30
2932.7555	2933.5305	0.77	−8.18	0.92	4.80E+04	5.42E+03	−7.04E+07	7.95E+06	6.892	1.432	5.300	0.016	258.48	46.29	431	4.63
2933.5319	2934.3083	0.78	−10.82	0.34	6.35E+04	1.99E+03	−9.31E+07	2.93E+06	7.320	1.566	5.256	0.016	387.06	48.25	430	4.50
2934.3097	2935.0861	0.78	124.38	0.34	−7.30E+05	1.97E+03	1.07E+09	2.88E+06	3.488	0.150	5.388	0.001	0.00	1.69	430	4.97
2935.0874	2935.8624	0.77	−42.71	1.52	2.51E+05	8.93E+03	−3.68E+08	1.31E+07	10.290	2.372	5.321	0.017	198.06	51.00	432	14.06
2935.8638	2936.6402	0.78	−7.78	0.39	4.57E+04	2.29E+03	−6.71E+07	3.36E+06	7.600	2.449	5.383	0.024	14.70	69.25	430	10.62
2936.6416	2937.4180	0.78	−47.15	1.77	2.77E+05	1.04E+04	−4.07E+08	1.53E+07	3.902	7.193	5.336	0.137	154.25	401.17	306	45.19
2937.4194	2938.1943	0.77	−31.84	0.23	1.87E+05	1.38E+03	−2.75E+08	2.02E+06	5.698	6.495	5.243	0.087	429.60	257.00	343	85.74
2938.1957	2938.9721	0.78	25.31	2.49	−1.49E+05	1.46E+04	2.19E+08	2.15E+07	11.814	4.149	5.245	0.027	421.03	79.49	430	48.14
2938.9735	2939.7499	0.78	−1.99	0.55	1.17E+04	3.24E+03	−1.72E+07	4.76E+06	10.015	3.673	5.400	0.027	−34.41	78.41	430	22.84
2939.7513	2940.5262	0.77	2.51	0.88	−1.48E+04	5.18E+03	2.17E+07	7.61E+06	9.115	3.217	5.430	0.026	−122.63	76.34	431	23.37
2940.5276	2941.3040	0.78	−4.51	6.69	2.65E+04	3.93E+04	−3.90E+07	5.78E+07	8.309	3.383	5.347	0.030	125.27	88.71	430	20.35
2941.3054	2942.0818	0.78	0.74	0.86	−4.37E+03	5.07E+03	6.43E+06	7.46E+06	−6.042	3.457	5.470	0.041	−239.98	120.83	430	19.12
2942.0832	2942.8581	0.77	16.63	2.65	−9.79E+04	1.56E+04	1.44E+08	2.29E+07	−3.602	3.018	5.580	0.062	−563.59	181.67	431	18.05
2942.8595	2943.6359	0.78	5.91	0.30	−3.48E+04	1.78E+03	5.12E+07	2.61E+06	6.416	2.848	5.323	0.033	191.55	96.82	424	15.96
2943.6373	2944.4137	0.78	−4.94	0.35	2.91E+04	2.05E+03	−4.28E+07	3.02E+06	10.966	2.929	5.239	0.021	439.01	60.73	309	14.57
2944.4151	2945.1901	0.77	2.41	1.49	−1.42E+04	8.78E+03	2.09E+07	1.29E+07	10.673	2.979	5.297	0.021	270.53	61.78	431	16.04
2945.1914	2945.9678	0.78	8.80	1.04	−5.19E+04	6.12E+03	7.64E+07	9.02E+06	7.049	3.309	5.454	0.034	−194.04	99.28	430	18.14
2945.9692	2946.7456	0.78	−2.73	1.11	1.61E+04	6.53E+03	−2.37E+07	9.62E+06	5.965	2.963	5.565	0.036	−521.14	106.68	430	16.44
2946.7470	2947.5220	0.77	8.56	2.02	−5.04E+04	1.19E+04	7.43E+07	1.75E+07	7.569	3.089	5.394	0.029	−17.17	86.84	431	17.45
2947.5233	2948.2997	0.78	−9.72	0.96	5.73E+04	5.66E+03	−8.44E+07	8.35E+06	11.689	2.446	5.280	0.016	317.16	46.79	430	15.93
2948.3011	2949.0775	0.78	2.53	1.44	−1.49E+04	8.50E+03	2.20E+07	1.25E+07	9.862	3.094	5.333	0.023	162.11	68.40	430	17.09
2949.0789	2949.7469	0.67	9.56	1.07	−5.64E+04	6.33E+03	8.32E+07	9.33E+06	7.684	3.774	5.395	0.035	−19.06	103.75	385	17.64
2955.0440	2956.0731	1.03	−2.62	1.00	1.55E+04	5.93E+03	−2.29E+07	8.77E+06	12.264	2.403	5.368	0.014	61.09	40.79	581	24.63
2956.0745	2956.8495	0.77	−15.37	0.77	9.09E+04	4.54E+03	−1.34E+08	6.72E+06	16.820	2.900	5.331	0.013	170.16	37.87	307	17.42
2956.8509	2957.6273	0.78	0.67	1.41	−3.99E+03	8.33E+03	5.89E+06	1.23E+07	15.218	3.003	5.325	0.015	186.27	43.22	430	18.42
2957.6286	2958.4050	0.78	7.40	2.37	−4.38E+04	1.40E+04	6.47E+07	2.07E+07	15.357	3.801	5.311	0.018	227.97	53.93	430	22.37
2958.4064	2959.1814	0.77	22.57	1.21	−1.34E+05	7.15E+03	1.98E+08	1.06E+07	9.905	3.263	5.500	0.024	−329.40	70.43	431	20.97
2959.1828	2959.9591	0.78	237.19	1.43	−1.40E+06	8.47E+03	2.08E+09	1.25E+07	−2.830	4.089	5.279	0.108	324.63	319.74	430	28.05
2959.9605	2960.7369	0.78	−1.85	1.80	1.09E+04	1.06E+04	−1.61E+07	1.57E+07	5.804	2.860	5.643	0.055	2786.40	162.34	430	44.58
2960.7383	2961.5133	0.77	−187.89	0.49	1.11E+06	2.90E+03	−1.65E+09	4.29E+06	12.141	9.469	5.763	0.055	−1110.48	162.45	431	162.90
2961.5147	2962.5730	1.06	0.14	0.69	−8.38E+02	4.08E+03	1.26E+06	6.04E+06	−13.302	4.825	5.235	0.039	−0.44	0.04	602	175.33

Notes.
[a] BJD–2457000.
[b] Degree of freedom of the fit.
[c] Fitted reduced chi-square.

Table A2
Eclipse Parameters and $O-C$ Analysis of the Quiescence of HS 2325+8205

Minima BJD (BJD–2457000)	Err. (day)	Minima Flux ($e\,s^{-1}$)	Err. ($e\,s^{-1}$)	Eclipse Depth ($e\,s^{-1}$)	E	$O-C$ (day)	Minima BJD (BJD–2457000)	Err. (day)	Minima Flux ($e\,s^{-1}$)	Err. ($e\,s^{-1}$)	Eclipse Depth ($e\,s^{-1}$)	E	$O-C$ (day)
2748.04965	0.00047	−21.96	3.43	18.69	4911	−0.00451	2923.14741	0.00054	−13.06	1.23	12.48	5812	−0.00236
2748.24578	0.00097	−16.84	3.81	15.32	4912	−0.00271	2923.72959	0.00068	−11.23	1.74	11.37	5815	−0.00318
2748.43980	0.00077	−18.10	3.87	17.89	4913	−0.00303	2923.92478	0.00166	−9.97	3.11	8.87	5816	−0.00233
2748.63278	0.00067	−20.12	3.45	19.41	4914	−0.00438	2924.11897	0.00128	−11.00	2.49	9.63	5817	−0.00247
2748.83026	0.00157	−17.29	3.47	17.20	4915	−0.00124	2924.31316	0.00085	−11.86	3.24	10.88	5818	−0.00262
2749.02389	0.00101	−17.22	3.58	16.16	4916	−0.00194	2924.50516	0.00088	−11.86	2.29	10.56	5819	−0.00495
2749.21852	0.00080	−18.97	2.77	18.66	4917	−0.00165	2924.70201	0.00073	−13.30	1.68	12.32	5820	−0.00243
2749.41425	0.00107	−25.02	3.86	23.07	4918	−0.00025	2924.89448	0.00073	−12.94	1.65	12.51	5821	−0.00430
2749.60627	0.00057	−25.82	2.99	22.76	4919	−0.00257	2925.09088	0.00156	−10.41	1.61	9.29	5822	−0.00223
2749.80051	0.00082	−24.11	3.67	23.67	4920	−0.00266	2925.28401	0.00094	−9.64	1.71	8.70	5823	−0.00344
2749.99575	0.00103	−21.31	3.80	21.68	4921	−0.00175	2925.47658	0.00106	−7.19	1.63	7.19	5824	−0.00520
2750.18884	0.00065	−19.97	3.31	19.95	4922	−0.00300	2925.67411	0.00195	−4.45	1.48	3.15	5825	−0.00201
2750.38168	0.00047	−22.28	3.03	22.40	4923	−0.00449	2925.86824	0.00114	−5.33	1.38	4.13	5826	−0.00221
2750.57743	0.00099	−17.82	3.61	14.40	4924	−0.00308	2926.06046	0.00081	−6.66	1.76	6.25	5827	−0.00433
2750.77369	0.00081	−15.51	2.63	13.96	4925	−0.00115	2926.25977	0.00228	−7.24	1.70	6.08	5828	0.00065
2750.96527	0.00057	−20.75	2.83	19.89	4926	−0.00391	2926.45165	0.00119	−8.91	1.47	8.69	5829	−0.00181
2751.16133	0.00101	−20.17	3.96	19.96	4927	−0.00218	2926.64694	0.00061	−10.85	1.33	9.42	5830	−0.00085
2751.35439	0.00118	−17.21	3.20	17.54	4928	−0.00346	2926.84007	0.00059	−11.38	1.41	11.01	5831	−0.00206
2751.54840	0.00215	−17.26	3.46	14.26	4929	−0.00378	2927.03478	0.00060	−12.06	1.55	11.33	5832	−0.00168
2751.74390	0.00082	−16.32	2.54	14.61	4930	−0.00262	2927.22958	0.00060	−13.02	1.62	12.08	5833	−0.00122
2751.93576	0.00085	−15.55	3.26	15.04	4931	−0.00509	2927.42332	0.00055	−15.66	1.44	14.63	5834	−0.00181
2752.13182	0.00067	−14.87	2.83	14.10	4932	−0.00337	2927.61774	0.00054	−15.24	1.57	14.18	5835	−0.00173
2752.32675	0.00085	−17.41	3.38	15.11	4933	−0.00277	2927.81199	0.00048	−15.35	1.54	15.37	5836	−0.00181
2752.52385	0.00084	−17.37	2.82	16.58	4934	−0.00001	2928.00528	0.00043	−14.52	1.26	13.93	5837	−0.00286
2752.71458	0.00066	−19.48	3.55	19.24	4935	−0.00361	2928.20064	0.00047	−11.25	1.28	10.45	5838	−0.00183
2752.91075	0.00116	−16.10	3.73	15.84	4936	−0.00178	2928.39362	0.00046	−9.96	1.44	9.50	5839	−0.00319
2753.10515	0.00080	−17.75	3.29	16.00	4937	−0.00171	2928.58864	0.00051	−11.34	1.59	10.24	5840	−0.00250
2753.29912	0.00101	−21.72	3.38	18.44	4938	−0.00208	2928.78288	0.00050	−10.53	1.47	9.29	5841	−0.00259
2753.49289	0.00056	−24.35	2.88	22.97	4939	−0.00264	2928.97731	0.00048	−12.66	1.62	11.83	5842	−0.00250
2753.68608	0.00080	−23.68	3.48	22.98	4940	−0.00379	2929.17042	0.00048	−14.32	1.47	13.96	5843	−0.00372
2753.88198	0.00067	−21.90	2.85	21.66	4941	−0.00222	2929.36408	0.00054	−14.62	1.56	14.56	5844	−0.00440
2754.07636	0.00054	−22.76	2.99	22.43	4942	−0.00217	2929.55701	0.00064	−13.58	1.38	12.31	5845	−0.00580
2754.26920	0.00059	−21.67	3.48	20.81	4943	−0.00367	2929.75128	0.00071	−12.99	1.21	11.31	5846	−0.00587
2754.46355	0.00041	−21.24	2.59	18.02	4944	−0.00365	2929.94547	0.00163	−7.52	1.51	6.70	5847	−0.00601
2754.65800	0.00054	−18.90	2.97	17.74	4945	−0.00354	2930.14159	0.00042	−8.36	1.01	7.05	5848	−0.00423
2754.85240	0.00042	−21.68	1.94	19.93	4946	−0.00347	2930.53097	0.00065	−6.34	1.08	5.36	5850	−0.00352
2755.04731	0.00064	−23.29	3.09	22.76	4947	−0.00290	2930.72632	0.00087	−6.66	1.45	7.00	5851	−0.00250
2755.24130	0.00097	−22.44	3.10	22.08	4948	−0.00324	2930.92258	0.00093	−6.67	1.38	6.03	5852	−0.00058
2755.43578	0.00094	−23.75	3.16	21.46	4949	−0.00310	2931.11665	0.00084	−8.07	1.17	7.28	5853	−0.00084
2755.62961	0.00129	−20.05	2.41	16.91	4950	−0.00360	2931.31084	0.00099	−10.18	1.64	8.84	5854	−0.00099
2755.82614	0.00156	−12.79	2.69	12.37	4951	−0.00141	2931.50517	0.00059	−11.27	1.29	10.09	5855	−0.00099
2756.98983	0.00066	−20.71	2.75	18.27	4957	−0.00373	2931.69948	0.00101	−10.79	1.95	9.80	5856	−0.00102
2757.18498	0.00070	−19.68	2.92	17.68	4958	−0.00291	2931.89287	0.00040	−12.44	1.12	11.47	5857	−0.00196
2757.38224	0.00102	−16.33	2.92	15.26	4959	0.00001	2932.08672	0.00050	−15.55	1.43	14.32	5858	−0.00245
2757.57369	0.00073	−20.34	3.10	19.23	4960	−0.00287	2932.28175	0.00055	−15.10	1.50	14.77	5859	−0.00175
2757.76961	0.00069	−20.14	2.76	21.02	4961	−0.00128	2932.47518	0.00047	−14.46	1.38	14.34	5860	−0.00266
2757.96156	0.00053	−24.15	2.96	25.25	4962	−0.00367	2932.66928	0.00050	−12.23	1.20	12.26	5861	−0.00289

Table A2
(Continued)

Minima BJD (BJD–2457000)	Err. (day)	Minima Flux ($e\,s^{-1}$)	Err. ($e\,s^{-1}$)	Eclipse Depth ($e\,s^{-1}$)	E	$O-C$ (day)	Minima BJD (BJD–2457000)	Err. (day)	Minima Flux ($e\,s^{-1}$)	Err. ($e\,s^{-1}$)	Eclipse Depth ($e\,s^{-1}$)	E	$O-C$ (day)
2758.15652	0.00039	−29.12	2.83	29.82	4963	−0.00304	2932.86454	0.00058	−9.70	1.53	9.14	5862	−0.00196
2758.35119	0.00083	−19.23	3.27	16.97	4964	−0.00271	2933.05832	0.00048	−11.03	1.63	9.78	5863	−0.00252
2758.54544	0.00088	−18.90	3.85	16.44	4965	−0.00279	2933.25213	0.00040	−11.90	1.52	10.88	5864	−0.00304
2758.73828	0.00046	−22.37	3.51	19.61	4966	−0.00429	2933.44533	0.00035	−10.43	1.06	9.12	5865	−0.00418
2758.93307	0.00054	−23.38	3.82	22.26	4967	−0.00383	2933.64018	0.00060	−10.45	1.64	9.87	5866	−0.00366
2759.12866	0.00088	−21.11	4.06	20.26	4968	−0.00258	2933.83523	0.00061	−12.68	1.56	12.29	5867	−0.00295
2759.32138	0.00055	−25.28	3.13	24.27	4969	−0.00419	2934.03044	0.00056	−13.21	1.18	12.55	5868	−0.00207
2759.51678	0.00104	−26.15	3.24	24.26	4970	−0.00313	2934.22300	0.00053	−15.49	1.23	14.48	5869	−0.00385
2759.70951	0.00084	−22.59	3.17	21.82	4971	−0.00473	2934.41680	0.00066	−14.71	1.54	14.12	5870	−0.00438
2759.90342	0.00036	−22.54	2.18	22.37	4972	−0.00516	2942.38812	0.00241	−10.71	3.65	9.83	5911	−0.00079
2760.10069	0.00184	−10.95	2.59	9.01	4973	−0.00222	2942.58147	0.00276	−11.88	3.57	11.36	5912	−0.00177
2760.29357	0.00072	−17.07	3.03	14.09	4974	−0.00368	2942.77686	0.00151	−16.43	3.07	13.81	5913	−0.00072
2760.48695	0.00045	−15.61	2.53	14.02	4975	−0.00463	2942.97188	0.00089	−20.82	2.59	17.89	5914	−0.00003
2760.68196	0.00124	−10.74	3.62	9.95	4976	−0.00396	2943.16433	0.00118	−18.89	3.60	17.46	5915	−0.00192
2760.87991	0.00141	−13.05	3.63	12.35	4977	−0.00034	2943.35972	0.00143	−18.34	3.42	17.72	5916	−0.00086
2761.07346	0.00096	−17.00	3.30	16.75	4978	−0.00113	2943.55289	0.00111	−18.06	3.99	17.76	5917	−0.00203
2761.26718	0.00087	−15.95	3.00	16.05	4979	−0.00174	2943.93918	0.00216	−21.25	3.52	19.23	5919	−0.00441
2761.46157	0.00084	−17.85	3.23	15.61	4980	−0.00169	2944.13654	0.00075	−24.03	3.81	23.69	5920	−0.00138
2761.65772	0.00113	−19.39	3.83	17.70	4981	0.00013	2944.32897	0.00079	−23.51	3.67	21.95	5921	−0.00328
2761.85170	0.00091	−26.31	4.09	22.02	4982	−0.00022	2944.52452	0.00064	−17.69	2.28	16.98	5922	−0.00207
2762.04507	0.00103	−21.80	3.23	18.44	4983	−0.00119	2944.71907	0.00122	−16.05	3.36	14.98	5923	−0.00185
2762.23769	0.00049	−22.56	2.30	22.74	4984	−0.00290	2944.91234	0.00109	−16.93	2.98	14.79	5924	−0.00292
2762.43284	0.00052	−22.68	2.25	24.07	4985	−0.00209	2945.10793	0.00094	−18.84	2.83	17.62	5925	−0.00166
2762.62501	0.00058	−24.96	3.96	26.38	4986	−0.00425	2945.29957	0.00077	−20.25	2.89	18.59	5926	−0.00436
2762.82078	0.00040	−25.70	2.91	25.07	4987	−0.00282	2945.49446	0.00120	−17.25	3.52	16.46	5927	−0.00380
2763.01470	0.00055	−19.72	3.16	18.80	4988	−0.00323	2945.68867	0.00089	−17.48	3.33	17.29	5928	−0.00393
2763.20932	0.00045	−19.95	3.15	16.88	4989	−0.00295	2945.88274	0.00060	−16.75	2.79	15.84	5929	−0.00419
2763.40369	0.00044	−17.67	2.60	15.87	4990	−0.00291	2946.07712	0.00121	−9.94	2.73	8.98	5930	−0.00415
2763.59706	0.00055	−25.52	3.96	21.93	4991	−0.00388	2946.27196	0.00098	−11.59	2.52	11.77	5931	−0.00364
2763.79231	0.00064	−20.11	2.89	20.57	4992	−0.00296	2946.47007	0.00159	−12.73	3.24	10.85	5932	0.00013
2763.98505	0.00053	−25.06	2.52	24.17	4993	−0.00456	2946.66503	0.00149	−17.82	4.35	16.01	5933	0.00076
2764.18017	0.00077	−23.64	2.66	22.31	4994	−0.00377	2946.85531	0.00082	−17.34	3.18	15.64	5934	−0.00330
2916.15166	0.00067	−12.98	1.63	11.73	5776	−0.00206	2947.05224	0.00090	−17.34	2.77	15.16	5935	−0.00070
2916.34539	0.00073	−12.65	1.60	10.85	5777	−0.00266	2947.24549	0.00120	−17.23	4.31	16.34	5936	−0.00179
2916.54014	0.00062	−12.77	1.35	12.26	5778	−0.00225	2947.44141	0.00088	−19.69	3.23	18.84	5937	−0.00020
2916.73133	0.00045	−13.17	1.31	13.81	5779	−0.00539	2947.63420	0.00086	−25.62	4.15	23.54	5938	−0.00175
2917.12045	0.00062	−11.17	1.41	10.40	5781	−0.00494	2947.82812	0.00092	−22.07	3.78	21.37	5939	−0.00216
2917.31567	0.00061	−9.41	1.28	8.51	5782	−0.00405	2948.02115	0.00078	−21.93	3.52	20.57	5940	−0.00347
2917.51042	0.00033	−9.74	1.06	8.94	5783	−0.00364	2948.21625	0.00067	−21.82	3.41	19.19	5941	−0.00270
2917.70551	0.00075	−9.05	1.59	7.94	5784	−0.00288	2948.41086	0.00083	−19.16	3.79	18.09	5942	−0.00242
2917.90111	0.00092	−9.46	1.47	7.99	5785	−0.00162	2948.60521	0.00114	−16.55	4.07	14.84	5943	−0.00241
2918.09541	0.00074	−10.47	1.39	9.41	5786	−0.00165	2948.79783	0.00061	−21.49	3.96	19.04	5944	−0.00412
2918.28972	0.00069	−9.84	1.17	8.93	5787	−0.00168	2948.99211	0.00075	−18.17	2.78	16.30	5945	−0.00418
2918.48471	0.00105	−9.99	1.73	9.35	5788	−0.00102	2949.18803	0.00127	−17.02	3.47	16.20	5946	−0.00259
2918.67809	0.00090	−11.73	1.44	11.34	5789	−0.00198	2949.38115	0.00132	−17.67	3.79	17.28	5947	−0.00381
2918.87212	0.00050	−14.61	1.26	13.51	5790	−0.00228	2949.57569	0.00157	−15.43	3.40	15.45	5948	−0.00360
2919.06629	0.00059	−13.86	1.34	12.58	5791	−0.00245	2955.21221	0.00077	−21.81	3.93	21.17	5977	−0.00279

Table A2
(Continued)

Minima BJD (BJD–2457000)	Err. (day)	Minima Flux ($e\ s^{-1}$)	Err. ($e\ s^{-1}$)	Eclipse Depth ($e\ s^{-1}$)	E	$O-C$ (day)	Minima BJD (BJD–2457000)	Err. (day)	Minima Flux ($e\ s^{-1}$)	Err. ($e\ s^{-1}$)	Eclipse Depth ($e\ s^{-1}$)	E	$O-C$ (day)
2919.26150	0.00055	−13.15	1.36	13.16	5792	−0.00157	2955.40790	0.00118	−20.50	3.40	18.05	5978	−0.00144
2919.45384	0.00054	−12.64	1.53	12.14	5793	−0.00357	2955.60228	0.00088	−20.76	3.79	20.28	5979	−0.00139
2919.64851	0.00049	−12.41	1.55	12.02	5794	−0.00323	2955.79743	0.00120	−21.04	3.36	21.11	5980	−0.00058
2919.84409	0.00050	−11.23	1.23	10.42	5795	−0.00199	2955.98975	0.00065	−24.62	3.28	24.70	5981	−0.00259
2920.03730	0.00066	−11.08	1.61	9.78	5796	−0.00311	2956.18381	0.00099	−25.88	4.01	24.57	5982	−0.00286
2920.23160	0.00051	−10.69	1.16	9.82	5797	−0.00315	2956.57246	0.00047	−28.39	3.46	27.33	5984	−0.00288
2920.42589	0.00065	−11.04	1.66	10.29	5798	−0.00319	2956.76733	0.00047	−22.82	2.86	21.81	5985	−0.00235
2920.61895	0.00052	−11.48	1.48	11.42	5799	−0.00447	2956.96045	0.00044	−20.98	3.17	19.62	5986	−0.00356
2920.81362	0.00059	−11.33	1.44	11.29	5800	−0.00413	2957.15473	0.00050	−18.70	3.40	17.09	5987	−0.00362
2921.00711	0.00045	−11.31	0.98	10.21	5801	−0.00497	2957.35082	0.00105	−16.06	4.34	15.10	5988	−0.00186
2921.20221	0.00066	−9.90	1.27	9.18	5802	−0.00421	2957.54381	0.00122	−20.99	5.40	19.16	5989	−0.00321
2921.39641	0.00195	−5.88	0.98	4.11	5803	−0.00434	2957.73702	0.00057	−24.35	3.20	23.83	5990	−0.00433
2921.59025	0.00180	−5.96	0.99	4.69	5804	−0.00484	2957.93126	0.00069	−27.98	3.53	27.49	5991	−0.00443
2921.78913	0.00332	−6.56	1.45	5.44	5805	−0.00029	2958.12642	0.00067	−26.39	2.63	25.40	5992	−0.00360
2921.98264	0.00093	−8.64	1.38	8.44	5806	−0.00112	2958.31989	0.00060	−25.92	2.44	23.03	5993	−0.00447
2922.17629	0.00068	−10.44	1.46	9.37	5807	−0.00180	2958.51565	0.00099	−20.34	2.79	17.75	5994	−0.00304
2922.37077	0.00068	−10.57	1.50	9.43	5808	−0.00166	2958.71039	0.00117	−14.95	3.01	12.61	5995	−0.00264
2922.56452	0.00090	−9.95	1.70	9.43	5809	−0.00224	2958.90284	0.00085	−13.15	2.89	11.13	5996	−0.00452
2922.75983	0.00065	−12.88	1.46	11.00	5810	−0.00127	2959.09804	0.00084	−15.99	2.97	15.44	5997	−0.00366
2922.95440	0.00070	−11.33	1.25	10.63	5811	−0.00103	…	…	…	…	…	…	…

ORCID iDs

Li-Ying Zhu https://orcid.org/0000-0002-0796-7009
Min-Yu Li https://orcid.org/0000-0002-8564-8193

References

Abraham, Z. 2018, NatAs, 2, 443
Applegate, J. H. 1992, ApJ, 385, 621
Armstrong, E., Patterson, J., Michelsen, E., et al. 2013, MNRAS, 435, 707
Aungwerojwit, A., Gänsicke, B., Rodríguez-Gil, P., et al. 2005, A&A, 443, 995
Barrett, P., O'Donoghue, D., & Warner, B. 1988, MNRAS, 233, 759
Bonnet-Bidaud, J. M., Motch, C., & Mouchet, M. 1985, A&A, 143, 313
Borkovits, T., & Hegedüs, T. 1996, A&AS, 120, 63
Boyd, D. R. S., de Miguel, E., Patterson, J., et al. 2017, MNRAS, 466, 3417
Bruch, A. 2022, MNRAS, 514, 4718
Bruch, A. 2023a, MNRAS, 519, 352
Bruch, A. 2023b, MNRAS, 525, 1953
Bruch, A. 2024, ApJS, 273, 6
Caproni, A., & Abraham, Z. 2004, ApJ, 602, 625
Cleveland, W. S. 1979, JASA, 74, 829
Court, J., Scaringi, S., Littlefield, C., et al. 2020, MNRAS, 494, 4656
Cui, Y., Hada, K., Kawashima, T., et al. 2023, Natur, 621, 711
De Miguel, E., Patterson, J., Cejudo, D., et al. 2016, MNRAS, 457, 1447
Foulkes, S. B., Haswell, C. A., & Murray, J. R. 2010, MNRAS, 401, 1275
Giacconi, R., Gursky, H., Kellogg, E., et al. 1973, ApJ, 184, 227
Hagen, H.-J., Groote, D., Engels, D., & Reimers, D. 1995, A&AS, 111, 195
Hameury, J. M. 2020, AdSpR, 66, 1004
Hameury, J. M., & Lasota, J. P. 2017, A&A, 602, A102
Hardy, L. K., McAllister, M. J., Dhillon, V. S., et al. 2017, MNRAS, 465, 4968
Harvey, D., Skillman, D. R., Patterson, J., & Ringwald, F. 1995, PASP, 107, 551
Heil, C. E., & Walnut, D. F. 1989, SIAMR, 31, 628
Hjellming, R. M., & Johnston, K. J. 1981, ApJL, 246, L141
Iłkiewicz, K., Scaringi, S., Court, J. M. C., et al. 2021, MNRAS, 503, 4050
Irwin, J. B. 1952, ApJ, 116, 211
Jenkins, J. M., Twicken, J., & McCauliff, S. 2016, Proc. SPIE, 9913, 99133E
Katz, J. I. 1973, NPhS, 246, 87
Kimura, M., & Osaki, Y. 2021, PASJ, 73, 1225
Kimura, M., Osaki, Y., & Kato, T. 2020, PASJ, 72, 94
Kinemuchi, K., Barclay, T., Fanelli, M., et al. 2012, PASP, 124, 963
Larwood, J. 1998, MNRAS, 299, L32
Lasota, J.-P. 2001, NewAR, 45, 449
Lenz, P., & Breger, M. 2005, CoAst, 146, 53
Montgomery, M. M. 2009, MNRAS, 394, 1897
Montgomery, M. M. 2012, ApJL, 745, L25
Morgenroth, O. 1936, AN, 258, 265
Osaki, Y. 1989, PASJ, 41, 1005
Osaki, Y. 1996, PASP, 108, 39
Osaki, Y., & Kato, T. 2013, PASJ, 65, 95
Papaloizou, J. C. B., & Terquem, C. 1995, MNRAS, 274, 987
Patterson, J. 1999, in Disk Instabilities in Close Binary Systems: 25 Years of the Disk-Instability Model. (Frontiers Science Series) Vol. 26 ed. S. Mineshige & J. C. Wheeler (Tokyo: Universal Academy), 61
Patterson, J., Kemp, J., Saad, J., et al. 1997, PASP, 109, 468
Pyrzas, S., Gänsicke, B., Thorstensen, J., et al. 2012, PASP, 124, 204
Ramsay, G., Wood, M. A., Cannizzo, J. K., Howell, S. B., & Smale, A. 2017, MNRAS, 469, 950
Ricker, G., Winn, J., & Vanderspek, R. 2015, JATIS, 1, 014003
Rubinur, K., Das, M., Kharb, P., & Honey, M. 2017, MNRAS, 465, 4772
Schaefer, B. E. 2021, RNAAS, 5, 148
Shears, J., Poyner, G., Januszewski, R., & Miller, I. 2011, JBAA, 121, 273
Smak, J. 2013, AcA, 63, 109
Stefanov, S. Y., & Stefanov, A. K. 2023, MNRAS, 520, 3355
Sun, Q.-B., Qian, S.-B., & Li, M.-Y. 2023a, ApJ, 955, 135
Sun, Q.-B., Qian, S.-B., Zhu, L.-Y., et al. 2023b, MNRAS, 526, 3730
Sun, Q.-B., Qian, S.-B., Zhu, L.-Y., et al. 2024a, ApJ, 966, 83
Sun, Q.-B., Qian, S.-B., Zhu, L.-Y., et al. 2024b, ApJ, 962, 123
Sun, Q.-B., Qian, S.-B., Dong, A.-J., et al. 2022, NewA, 93, 101751
Sun, Q.-B., Qian, S.-B., Zhu, L.-Y., et al. 2023c, MNRAS, 518, 3901
Thomas, D. M., & Wood, M. A. 2015, ApJ, 803, 55
Twicken, J. D., Chandrasekaran, H., Jenkins, J. M., et al. 2010, Proc. SPIE, 7740, 77401U
Vogt, N. 1983, A&A, 128, 29
Warner, B. 1995, Cataclysmic Variable Stars (Cambridge: Cambridge Univ. Press), 28
Wood, M. A., & Burke, C. J. 2007, ApJ, 661, 1042
Wood, M. A., Thomas, D. M., & Simpson, J. C. 2009, MNRAS, 398, 2110